PNAS
www.pnas.org

Supplementary Information for

Experimental and Theoretical Evidence for Hydrogen Doping in Polymer Solution-Processed Indium Gallium Oxide

Wei Huang, Po-Hsiu Chien, Kyle McMillen, Sawankumar Patel, Joshua Tedesco, Li Zeng, Subhrangsu Mukherjee, Binghao Wang, Yao Chen, Gang Wang, Yang Wang, Yanshan Gao, Michael J. Bedzyk, Dean M. DeLongchamp, Yan-Yan Hu, Julia E. Medvedeva, Tobin J. Marks, Antonio Facchetti

* Michael J. Bedzyk, Dean DeLongchamp, Yan-Yan Hu, Julia E. Medvedeva, Tobin J. Marks, Antonio Facchetti
Email: bedzyk@northwestern.edu, dean.delongchamp@nist.gov, yhu@fsu.edu, juliaem@mst.edu, t-marks@northwestern.edu, a-facchetti@northwestern.edu

This PDF file includes:

Supplementary text
Figures S1 to S39
Tables S1 to S11
SI References

www.pnas.org/cgi/doi/10.1073/pnas.2007897117

Table of Contents

1. AFM and GIXRD of IGO:PVA films ... 3
2. XPS O 1s of IGO:PVA films ... 4
3. XPS C1s of IGO:PVA films ... 7
4. Transistor performance of IGO:PVA films ... 9
5. UV-vis and UPS analysis of IGO:PVA films ... 11
6. XRR analysis on IGO:PVA films ... 13
7. EXAFS analysis of IGO:PVA films ... 14
8. Proton NMR of PVA and SIMS depth profiles of IGO:PVA films ... 15
9. IGO:PVA powder and corresponding SS-NMR measurements ... 16
10. Theoretical Calculations on IGO with hydrogen doping ... 19
11. Role of Ga and PVA in IGO:PVA films ... 24
11.1. In_2O_3:PVA and IZO:PVA films ... 24
11.2 IGZO:PVA films ... 25
11.3 IGO:PVP films ... 26
11.4 IGO:Glycerol films ... 27

1. AFM and GIXRD of IGO:PVA films

The surface morphologies and texturing of IGO films with different PVA contents (from 0 wt.% to 14 wt.%) were assessed by AFM and GIXRD (Figures S1 and S2). A smooth semiconductor layer surface in a TFT typically enhances carrier transport since it minimizes charge scattering effects on the back channel.(1) The present result ($\sigma_{RMS} \leq 0.19$ nm) suggests that, independent of the PVA content, all the IGO:PVA films have the potential to form high-performance metal oxide transistors.

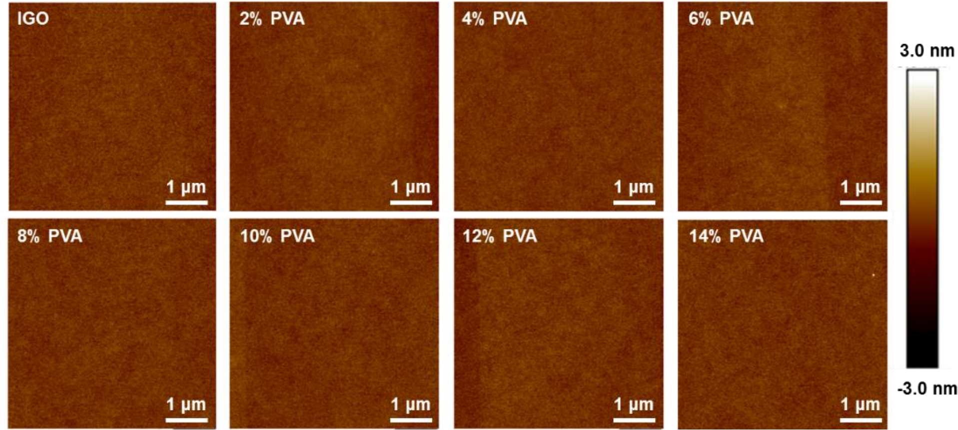

Figure S1. AFM images for IGO:PVA films with the indicated wt% PVA content of the precursor.

Table S1. RMS data for IGO:PVA films with different PVA contents in the precursors. All films are smooth with RMS roughness (σ_{RMS}) values ranging from 0.15 nm to 0.19 nm

PVA content (wt. %)	0	2	4	6	8	10	12	14
RMS (nm)	0.16	0.17	0.15	0.18	0.17	0.18	0.19	0.19

GIXRD was utilized to quantify the texturing of the IGO:PVA films. All IGO:PVA films are completely amorphous, which is in agreement with previous reports indicating that IGO films with a relatively large Ga content (> 20 wt. %) are amorphous when annealed at < 400 ºC.(2) Note that amorphous metal oxide films typically have uniform electrical performance over large areas and are more compatible with flexible substrates since they lack grain boundaries.(3)

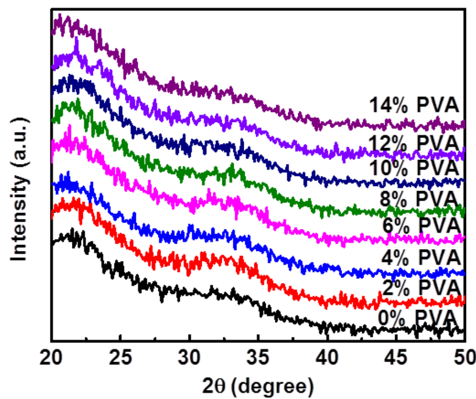

Figure S2. GIXRD for IGO:PVA films with the indicated wt% PVA content.

2. XPS O 1s of IGO:PVA films

Next, XPS was utilized to examine the local chemical environment of the IGO:PVA films. Oxygen 1s ionizations were first analyzed/deconvoluted based on the following criteria: 1) the M-O-M bonding feature is at 529.9±0.1 eV; 2) other oxygen species are at 531.4±0.1 eV. Uncertainties reported in peak positions are standard deviations obtained from peak fits to the spectra. As shown in Figure S3, adding more PVA to the IGO does not obviously influence the O 1s envelope, which always exhibits the major O 1s component due to M-O-M bonding at ≈529.9 eV. By fitting the O 1s peaks, the M-O-M, and other oxygen molar ratios can be quantified and are summarized in Figure 1c and Table S2. Importantly, increasing the PVA concentration in the IGO precursor from 0 wt.% to 8 wt.% does not significantly change the M-O-M lattice content (77.6% to 80.6%), however, greater PVA contents significantly suppress M-O-M formation to 70.1% (12 wt.% PVA) and 68.9% (14 wt.% PVA). Lowering the M-O-M content usually decreases charge transport in semiconducting MOs, however, since all of the present IGO:PVA films exhibit a relatively large M-O-M lattice content, there should be sufficient electron transporting pathways for efficient semiconductor functionality.

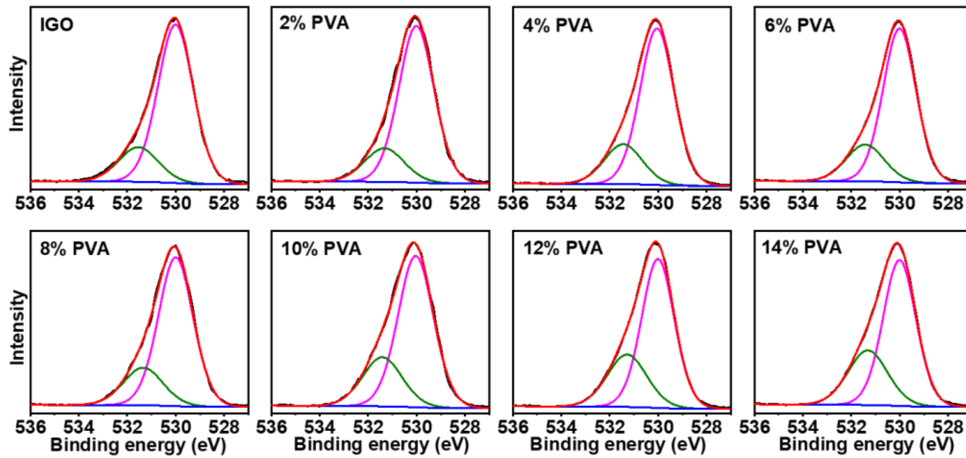

Figure S3. XPS O 1s for IGO:PVA films with different PVA content based on the assumption of 1) M-O-M bond at 529.9±0.1 eV; 2) other Oxygen species at 531.4±0.1 eV. Uncertainties in peak position are standard deviation obtained from peak fits to the spectra. Note that XPS was carried after surface Ar^+ etching of 1 nm to 2 nm.

Table S2. M-O-M, and other O species content in IGO:PVA films with different PVA contents in the precursors.

PVA content (wt. %)	0	2	4	6	8	10	12	14
M-O-M (at. %)	80.4	80.6	77.9	78.4	77.6	73.4	70.1	68.9
Other O (at. %)	19.6	19.4	22.1	21.6	22.4	26.6	29.9	31.1

Note that accurate XPS O 1s deconvolution assumes a pure metal oxide composition. However, for the present IGO:PVA films this may be challenging especially for binding energies higher than 531.0 eV, since pure PVA has O 1s signal in the range of 531.0 to 535.0 eV, and centered at 532.3 eV (Figure S4). Utilizing either of the two most frequently adopted ways to deconvolute the oxygen 1s peak in MOs (one assigns the M-O-M bond at 529.9±0.1 eV, oxygen vacancies (O_{vac}) at 531.0±0.1 eV and M-OH at 532.0±0.1 eV(4, 5), another assigns the M-O-M bond at 529.9±0.1 eV, M-OH bond at 531.2±0.1 eV; and M-OR, H_2O, or organic

oxygen species at 532.1±0.1 eV.(6-8)), similar trends are observed where less than 10 wt.% PVA in the precursor does not dramatically decrease the M-O-M content (Figures S5-S7).

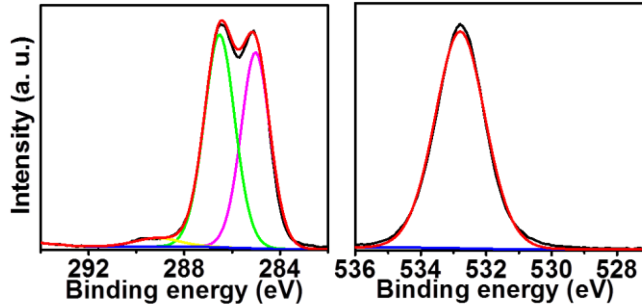

Figure S4. XPS C 1s and O 1s for pure PVA film.

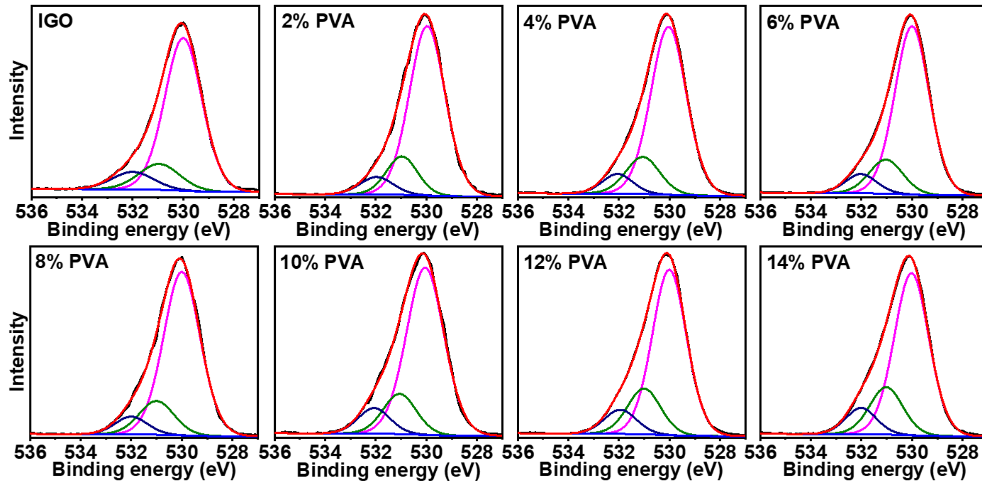

Figure S5. XPS O 1s for IGO:PVA films with different PVA content based on the assumption of M-O-M bond at 529.9±0.1 eV, Oxygen vacancies (O_{vac}) at 531.0±0.1 eV and M-OH at 532.0±0.1 eV. Note that XPS was carried after surface Ar^+ etching of 1 nm to 2 nm.

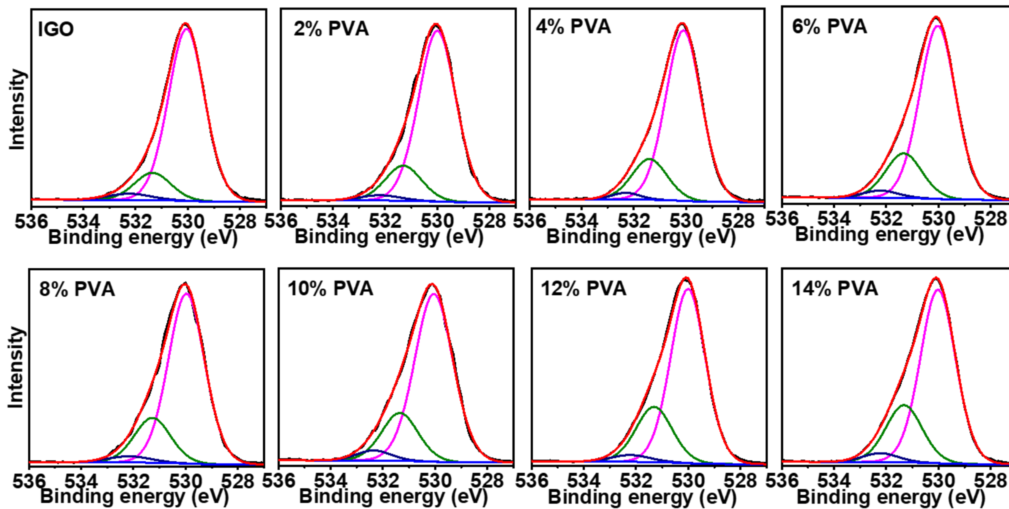

Figure S6. XPS O 1s for IGO:PVA films with the PVA contents indicated based on the assumption of M-O-M bond at 529.9±0.1 eV, M-OH bond at 531.2±0.1 eV; and M-OR, H_2O, or organic oxygen species at 532.1±0.1 eV. Note that XPS was carried after surface Ar^+ etching of 1 - 2 nm.

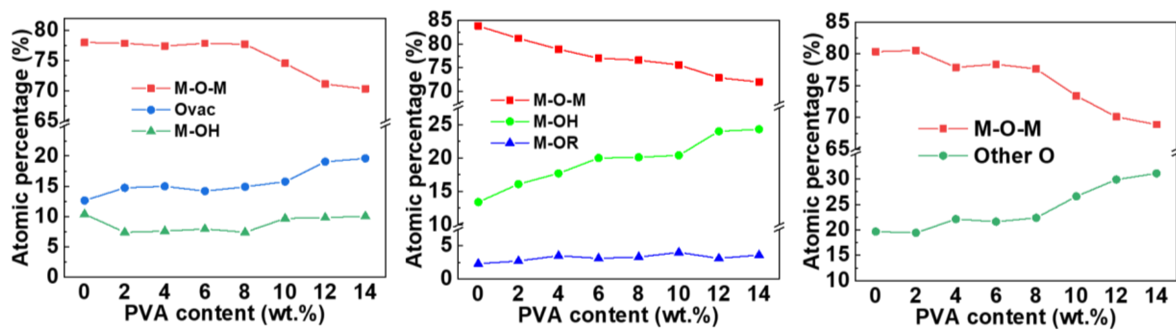

Figure S7. Summary of the relative O contents by fitting the XPS O 1s peaks of IGO:PVA films with different modeling assumptions.

3. XPS C1s of IGO:PVA films

To evaluate the degree to which the PVA polymeric chains remain intact after the films are thermally annealed at 300 °C, the XPS carbon 1s signals of IGO:PVA films were also acquired (Figure S8), and the atomic ratios of carbon, along with those of indium, gallium, and oxygen in the films, were calculated (Figure 1d and Table S3). As shown in Table S3, the In/Ga atomic ratio remains constant at about 6/4, while carbon content slowly increases as the PVA content increases, from 0.8 at.% at 0 wt.% PVA to 4.0 at.% at 14 wt.% PVA. Compared to the expected film carbon content assuming all the carbon in PVA precursor remains in the IGO films, the XPS detected carbon in the films is significantly lower and never exceeds 4.0 at.%. In contrast, the theoretical carbon content already exceeds 4.0 at.% with only 2 wt.% of PVA in the precursor, and increases to more than 20 at.% with 14 wt.% PVA.

IGO films without PVA only show a major carbon peak at 285.0 eV (C-C bond) and a week side peak at ≈287.0 eV (C-O and/or C=O bond), which is assigned to environmental carbon contamination. Note, due to the low intensity of the carbon 1s peaks in these films, it is difficult to achieve a reliable quantitative deconvolution between the C-O (286.5 eV) and C=O (287.7 eV) ionizations, since they both have binding energies at ≈287.0 eV. As shown in Figure S8, by increasing the PVA content in the blend from 2 wt.% to 14 wt.%, the peaks at 285.0 eV and 287.0 eV remain along with a new peak at ≈290.0 eV, which usually is assigned to an O-C=O bond type of carbon.(9) Since in pure PVA the carbon peaks are mainly located at 285.0 eV (C-C/C-H) and 286.5 eV (C-O) while the oxygen peak is at 532.3 eV (Figure S4), the new C 1s peak at 290.0 eV in the IGO:PVA films indicates that during the fabrication process (especially during 300 °C annealing), the PVA is substantially oxidized, accounting for the complicated C-O bonding pattern.(9, 10) Moreover, since the formation of the O-C=O (≈290.0 eV) from PVA seems unlikely, the C1s peaks without Ar^+ etching were also acquired for these films. As shown in Figure S9, without etching the films, large quantities of absorbed C on the surface, indicated by a main peak at ≈284.90 eV, are present. Interestingly, no peak at ≈290.0 eV is observed but only one at ≈288.7 eV having the highest binding energy. Based on the results of Figures S8-S9, it seems that Ar^+ etching shifts the carbon binding energies, making unambiguous analysis of the form of carbon in the IGO:PVA films challenging.

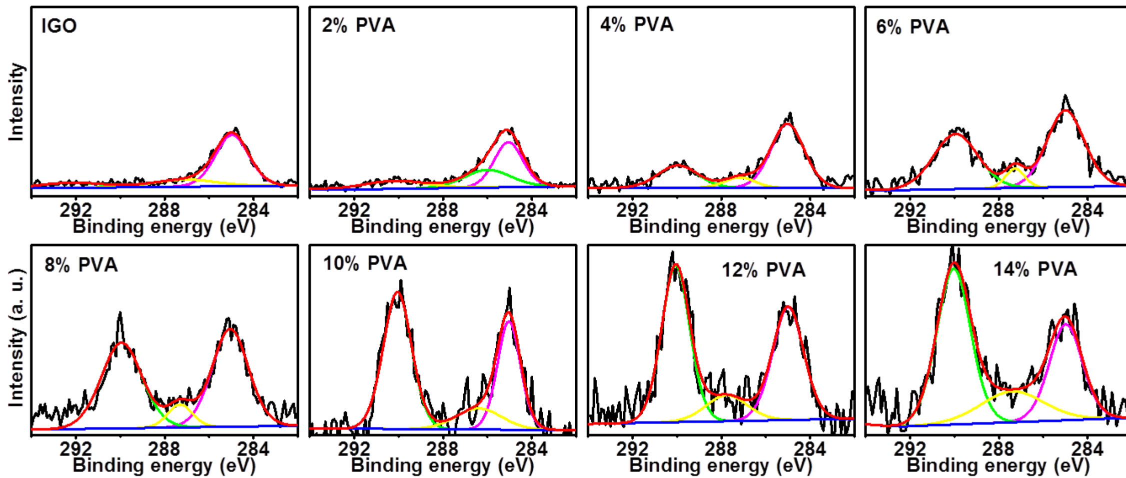

Figure S8. XPS C 1s for IGO:PVA films with the indicated PVA content after Argon etching (Fitting parameters: Shirley background type, Gauss-Lorentz peak type).

Table S3. Atomic percentage of In, Ga, O, and C in IGO:PVA films with different PVA content (T_{anneal} = 300 °C).

PVA content (wt.%)	0	2	4	6	8	10	12	14
In (at.%)	24.8	25.0	24.6	24.4	24.6	23.2	24.0	23.5
Ga (at.%)	17.5	17.1	17.5	17.4	17.2	17.8	17.0	17.2
O (at.%)	56.9	56.2	55.6	55.9	55.8	56.1	55.8	55.4
C (at.%)	0.8	1.6	2.3	2.3	2.4	2.9	3.3	4.0

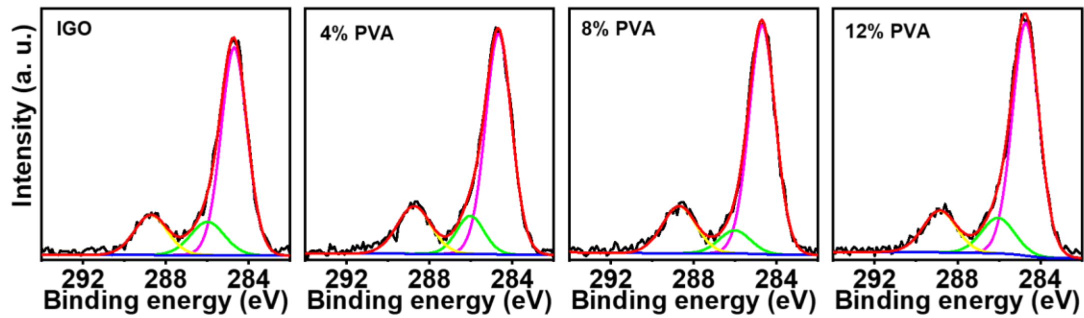

Figure S9. XPS C 1s for IGO:PVA films with different PVA content before Argon etching.

4. Transistor performance of IGO:PVA films

Table S4. Performance metrics of IGO:PVA TFTs with the indicated PVA content.

Annealing temp. (°C)	TFT	PVA concentration [wt.%]							
		0	2	4	6	8	10	12	14
300	μ [cm^2/Vs]	0.10±0.04	2.17±0.21	3.80±0.46	4.44±0.30	6.43±0.73	4.60±0.76	1.94±0.45	1.25±0.66
	V_T [V]	36.4±9.2	32.1±2.7	24.7±2.9	18.5±3.6	16.6±2.7	34.5±3.6	36.3±4.8	50.4±5.5
	I_{ON}/I_{OFF}	10^4	10^6	10^6~10^7	10^7	10^6~10^7	10^6~10^7	10^6	10^5~10^6
250	μ [cm^2/Vs]	0.01±0.02	0.38±0.14	2.56±0.26	0.60±0.13	0.08±0.01	0.03±0.01	0.005±0.001	0.003±0.001
	V_T [V]	40.0±10.2	29.1±8.5	17.8±3.6	22.2±5.8	35.6±6.3	41.3±7.2	42.7±5.6	46.2±6.3
	I_{ON}/I_{OFF}	10^7	10^7	10^7	10^7	10^7	10^7	10^6~10^7	10^6~10^7

* Average of more than 10 devices.

Table S5. Mobility comparison of IGO based transistors with indicted fabrication parameters.

	Mobility (cm^2/Vs)	Ga/In (atomic)	Fabrication method	Annealing temperature (°C)
Ref(11)	2.7	1.50	RF sputtering	RT
Ref(12)	9.5	0.33	ALD	300
Ref(13)	3.6	0.35	Spin-coating	500
Ref(14)	6.1	0.20	Spin-coating	500
Ref(15)	3.2	0.35	Spin-coating	350
Ref(16)	12.5	0.06	Spin-coating combustion	300
Ref(17)	3.8	0.25	Spin-coating	250
This work	6.4	0.67	Spin-coating	300
This work	2.6	0.67	Spin-coating	250

We also investigated a lower processing temperature of 250 °C for IGO:PVA films to assess whether the aforementioned TFT PVA doping-induced performance enhancement is preserved. As shown in Figure S10 and Table 1, upon PVA doping, a very large reduction in hysteresis from ≈ 40 V (0 wt% PVA) to less than 4 V (4 wt% PVA) is achieved. Furthermore, I_{ON} first increases from $3.47\pm3.89\times10^{-7}$ A (0 wt% PVA), to $8.47\pm0.78\times10^{-5}$ A (2 wt% PVA), to $8.69\pm0.41\times10^{-5}$ A (4 wt% PVA), and then decreases to $1.24\pm0.32\times10^{-4}$ A (6 wt% PVA), to $4.85\pm0.49\times10^{-4}$ A (10 wt% PVA), to $7.10\pm0.97\times10^{-4}$ A (14 wt% PVA). The performance of the 250 °C annealed IGO:PVA transistors (μ = 0.01 cm^2/Vs to 2.56 cm^2/Vs) is overall somewhat inferior to those annealed at 300 °C due to larger densities of charge traps. However, PVA incorporation from 0 wt.% to 4 wt.% (Figure S10) enlarges I_{ON} and reduces V_{TH} and hysteresis, with a maximum mobility of 2.56±0.26 cm^2/Vs and a minimum V_T of 17.8±3.6 V for 4 wt.% PVA. Compared to the 300 °C processed TFTs, the optimal PVA content yielding the highest mobility and lowest V_T shifts to a lower PVA content (from 8 wt.% to 4 wt.%). The amounts of residual carbon in the 250 °C annealed films are always higher than those after 300 °C annealing. For example, with only 4 wt.% of PVA in precursor, the carbon content in the IGO:PVA film is already 3.4 at.% with an annealing temperature of 250 °C, while for IGO:PVA films annealed at 300 °C, the carbon content remains lower than 2.9 at.% with up to 10 wt.% PVA in precursor. Even though PVA in the IGO precursor has the capacity to reduce the charge trap density in the resulting films, greater residual PVA in the films should also introduce more scattering sites, reduce the overall metal oxide density, leading to less effective charge transporting pathways. This agrees with the performance of IGO-based TFTs with greater than 8 wt.% (300 °C annealing temp.) or 4 wt.% (250 °C annealing temp.) PVA content, where decreasing I_{ON}, mobility, and positively shifted V_T are obtained with excess amounts of polymer in the MO precursors.

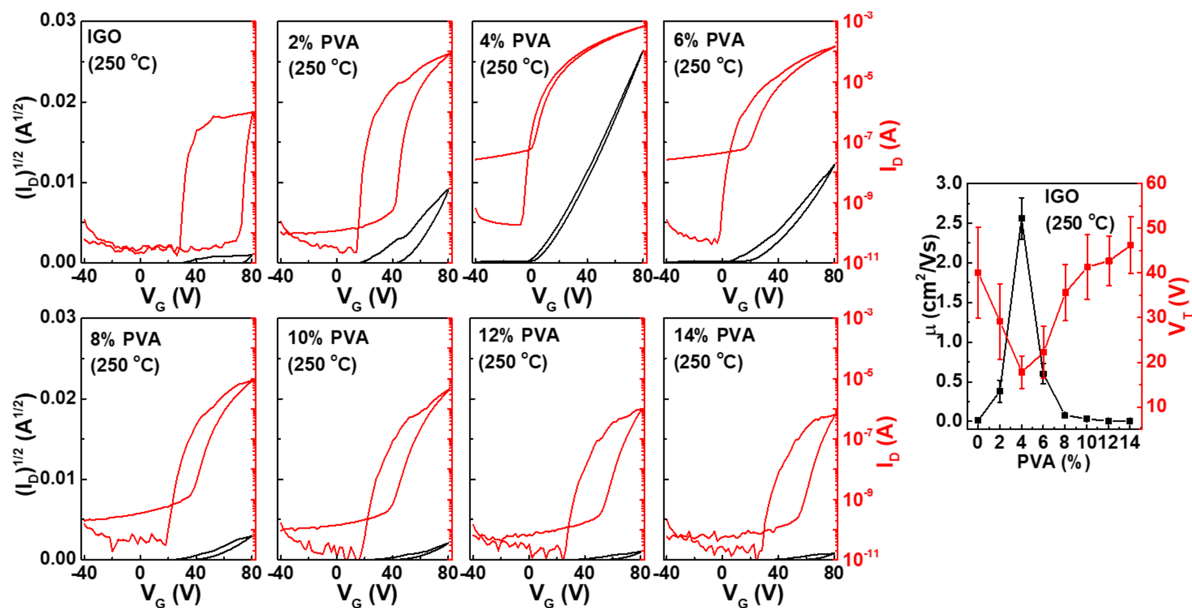

Figure S10. Representative transfer curves of TFTs based on IGO:PVA with different PVA contents (V_D = +80 V, annealing temperature 250 °C), along with calculated mobility and V_T of IGO:PVA TFTs.

Table S6. Atomic percentage of In, Ga, O, and C in IGO:PVA films with different PVA content (T_{anneal} = 250 °C).

PVA content (wt.%)	0	2	4	6	8	10	12	14
In (at.%)	23.6	23.5	22.9	22.0	21.8	21.6	21.9	21.2
Ga (at.%)	16.3	15.2	16.0	15.5	15.6	16.3	15.3	15.2
O (at.%)	59.0	58.7	58.6	58.5	58.2	57.5	57.6	57.8
C (at.%)	1.1	2.6	3.4	4.0	4.4	4.7	5.2	5.8

5. UV-vis and UPS analysis of IGO:PVA films

UV-vis spectroscopic and UPS measurements were carried out to study the electronic structure and the energy landscapes (Figures S11 and S12) of the IGO:PVA films. As the PVA content in the blend precursor is increased, the band gap increases from 3.02 eV (0 wt.% PVA) to 3.07 eV (8 wt.% PVA), to 3.11 eV (12 wt.% PVA), assuming an indirect band gap. Note, a similar trend is also observed, from 3.93 eV (0 wt.% PVA) to 3.97 eV (8 wt.% PVA), to 4.11 eV (12 wt.% PVA), assuming a direct band gap structure. Moreover, even though PVA has a large intrinsic band gap of about 6 eV (Figure S11), it should not contribute to any oxide band gap opening process by forming a new discrete compound, since the majority of the compound is IGO with only small amounts of PVA residue (Figure 1d). By excluding any effects of quantum confinement (Figure S13), it is then reasonable that PVA addition to the IGO precursor alters the electronic structure of the resulting IGO:PVA films.(18) More specifically, since the optical band gap of the semiconducting oxide represents the gap between valence band and Fermi level which is near/in the conduction band,(19) the band gap widening is more likely due to a Fermi level shift associated with a doping process induced by a PVA reaction with the IGO.(20-22) Next, the valence band and cut-off regions in the UPS spectra of the IGO:PVA films were measured, and the spectra are presented in Figure S12. The work function (WF) of neat IGO films is 4.21 eV and it first shifts to lower values as the PVA content is increased (4.11 eV for 8 wt.% PVA) and then decreases to ≈4.15 eV for larger PVA contents (10 wt.% - 14 wt.%). Detailed energy level information from the UV-vis and UPS data are summarized in Table S7. These data confirm an expansion in the energetic distance between valence band maximum (VBM) to Fermi level (E_F). Previous studies, including experimental and theoretical results, have shown similar results after hydrogen doping, where an up-shift of the E_F, and an enlarged gap between the VBM and E_F are observed.(21-23) Such an outcome reveals that PVA embedded in the IGO matrix can lower the WF (i.e., up-shift the E_F), demonstrating that PVA in the IGO precursor can function to electron dope the oxide. In addition, the PVA-induced electron doping also increases the density of states near the VBM, which may be related to minor carbon residues from the PVA. However, these sub-band gap states should not influence the electron transport, since they are mostly at least 1 eV away from E_F.

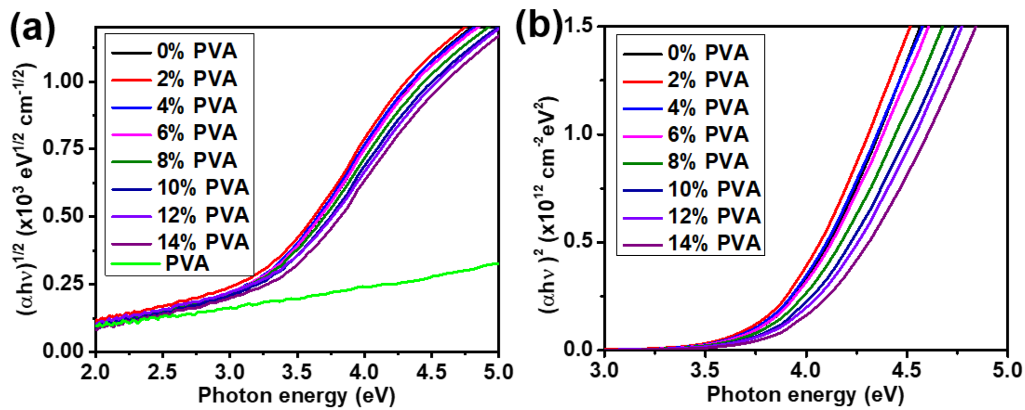

Figure S11. Tauc's plots of IGO:PVA films with different PVA contents, evaluated based on (a) indirect band gap, (b) direct band gap.

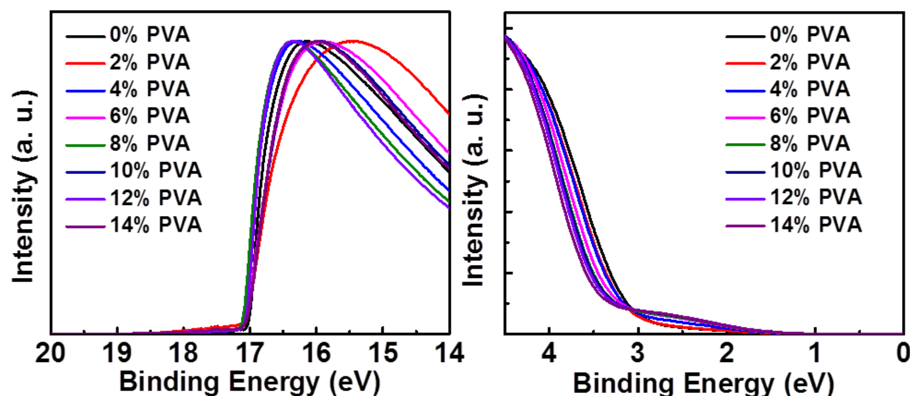

Figure S12. UPS measurements on IGO:PVA films with different PVA contents.

Quantum confinement effects may also enlarge the band gap since the thickness of IGO:PVA film decreases [see Figure S14 and Table S8, from 10.2 nm (0 wt.% PVA), to 9.4 nm (4 wt.% PVA), to 9.1 nm (8 wt.% PVA), 8.8 nm (12 wt.% PVA)].(24-26) To resolve the issue of whether the band gap opening process is induced by quantum confinement effects, we carried out a control experiment so that varying the PVA concentration does not alter the overall IGO:PVA film thickness (By using 16 mg/mL PVA solution instead of 8 mg/mL). In this experiment all IGO:PVA films have a constant thickness of 10.0 to 10.5 nm when the PVA contents varies from 0 wt.% to 14 wt.%, however note that the UV-vis spectrum (Figure S13) still evidences a band gap widening with increasing the PVA content.

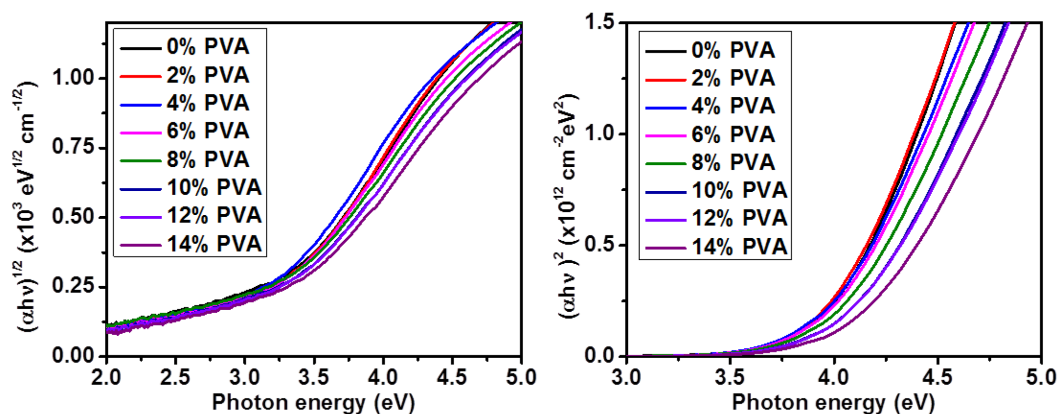

Figure S13. Tauc's plots of IGO:PVA films with different PVA contents, evaluated based on (a) indirect band gap, (b) direct band gap. Note, the PVA solution concentration used here is 16 mg/mL, instead of 8 mg/mL.

Table S7. Summary of IGO:PVA film energy levels based on UV-vis and UPS measurements.

PVA content (%wt)	0	2	4	6	8	10	12	14
Indirect band gap (eV)	3.02	2.99	3.02	3.05	3.07	3.09	3.11	3.14
Direct band gap (eV)	3.93	3.90	3.95	3.94	3.974.21	4.02	4.06	4.11
Work function (eV)	4.21	4.13	4.12	4.13	4.11	4.16	4.15	4.15
VBM-E_F (eV)	3.12	3.18	3.19	3.30	3.34	3.37	3.38	3.43

6. XRR analysis on IGO:PVA films

XRR measurements were carried out to analyze the semiconductor film microstructure, since MO TFT performance is sensitive to film thickness, electron density profile distribution, and surface roughness. Note that the reflectivity curves of the IGO:PVA films on Si/SiO_2 with different PVA contents are nearly indistinguishable (Figure S14), indicating that polymer addition to IGO does not produce dramatic variations in the film electron density profile. By carefully fitting the XRR curves, the electron density profiles were obtained and are plotted in Figure S14. Note, even though the films are fabricated with a three-layer spin-coating and annealing process, the electron density is very uniform across the layers (Figure S14) without any evidence of a layered structure as frequently seen for solution processed multilayer MO-polymer films.(27) The average film electron densities, thicknesses, and surface roughnesses are summarized in Table S8. As the PVA content in the precursor increases, the average electron density and film thickness gradually decrease from 1.42 e/ $Å^3$ and 10.2 nm (0 wt.% PVA) to 1.41 e/ $Å^3$ and 9.4 nm (4 wt.% PVA), to 1.39 e/ $Å^3$ and 9.1 nm (8 wt.% PVA), and to 1.30 e/ $Å^3$ and 8.8 nm (14 wt.% PVA), respectively. However, the film surface roughness remains in a small range (0.32 nm to 0.37 nm), which is in agreement with the AFM data.

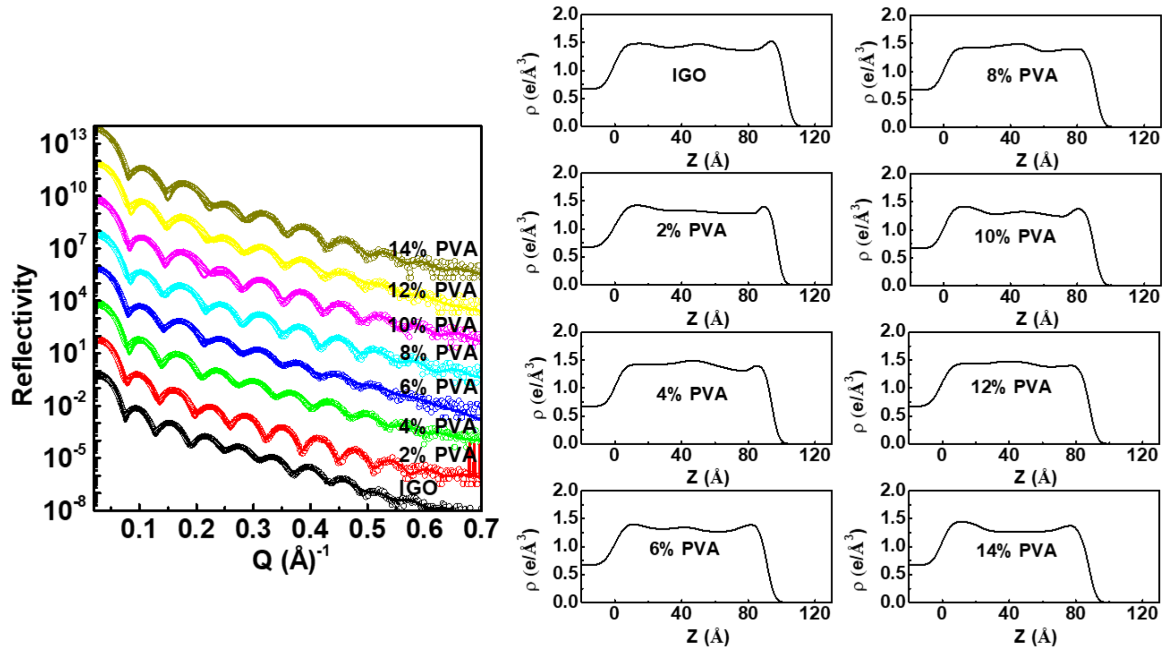

Figure S14. XRR measurements (open circles) and fits (solid lines) of IGO:PVA films with different PVA contents, along with fitted electron density profiles.

Table S8. Fitted thickness, average electron density, and surface roughness of IGO:PVA films based on the XRR measurements.

PVA (wt.%)	0	2	4	6	8	10	12	14
Thickness (nm)	10.2	9.7	9.4	9.1	9.1	9.0	8.8	8.8
Electron Density (e/Å^3)	1.42	1.42	1.41	1.41	1.39	1.32	1.31	1.30
Roughness (nm)	0.35	0.32	0.33	0.37	0.34	0.36	0.36	0.34

7. EXAFS analysis of IGO:PVA films

The incident beam energies were tuned to near the In K-edge or Ga K-edge to measure the EXAFS spectra. These exhibit the principal first shell absorption peaks at ≈2.14 Å and ≈1.85 Å, respectively. The 2nd shell of In-In proximity is relatively weak in all IGO:PVA films compared to polycrystalline In_2O_3, and is comparable to that of amorphous In_2O_3, while no 2nd Ga-Ga shell is observed.(28-31)

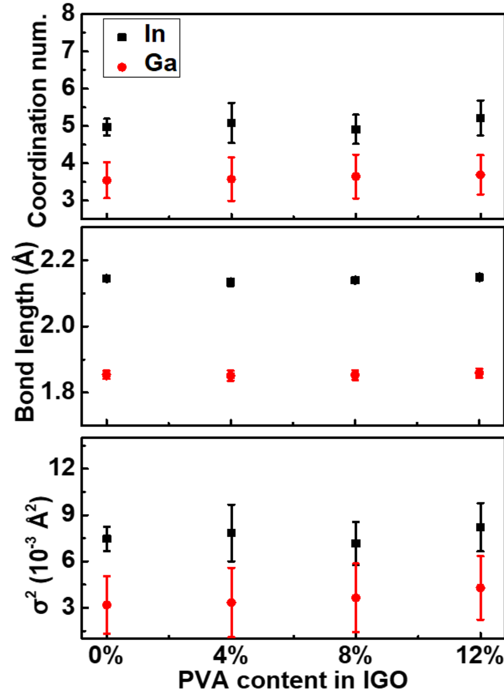

Figure S15. First shell coordination number, bond length, and σ^2 values of In and Ga, respectively, in IGO:PVA films.

Table S9. First coordination shell information from the In K-edge and Ga K-edge.

PVA (wt.%)	In K-edge			Ga K-edge		
	Coordination num.	Bond length (Å)	σ^2 (10^{-3} Å^2)	Coordination num.	Bond length (Å)	σ^2 (10^{-3} Å^2)
0	4.97±0.22	2.145±0.005	7.47±0.80	3.55±0.48	1.854±0.012	3.19±1.85
4	5.08±0.54	2.134±0.011	7.84±1.83	3.58±0.58	1.851±0.015	3.35±2.25
8	4.91±0.39	2.140±0.009	7.16±1.40	3.65±0.59	1.853±0.015	3.64±2.22
12	5.22±0.47	2.149±0.009	8.21±1.56	3.69±0.53	1.859±0.014	4.29±2.07

8. Proton NMR of PVA and SIMS depth profiles of IGO:PVA films

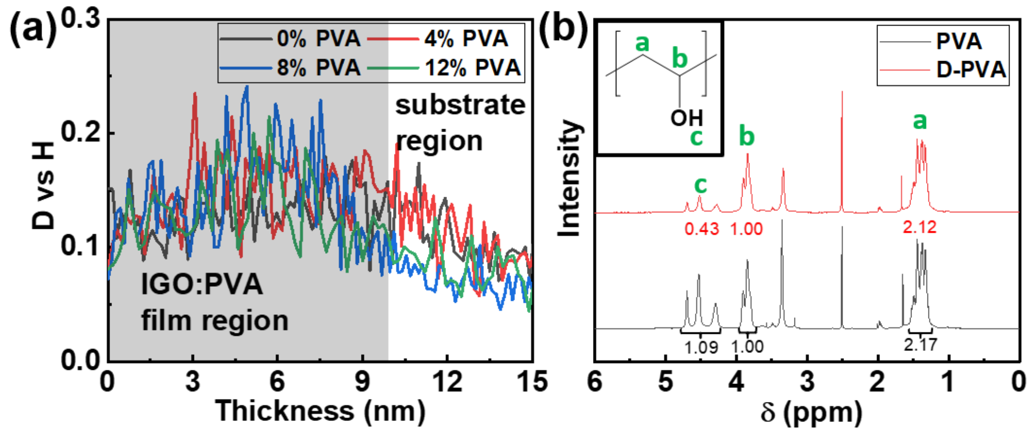

Figure S16. (a) D vs H obtained from ToF-SIMS depth profile of the IGO:PVA films fabricated on Si wafers with D_2O as the solvent. (b) Proton NMR of PVA (Note, ^{1}H-NMR spectra are recorded in deuterated DMSO, where **black** represents PVA directly dissolved in DMSO, and the **red line** represents PVA which was first dissolved in D_2O to obtain exchanged D-PVA, then this D-PVA was vacuum dried and dissolved in DMSO).

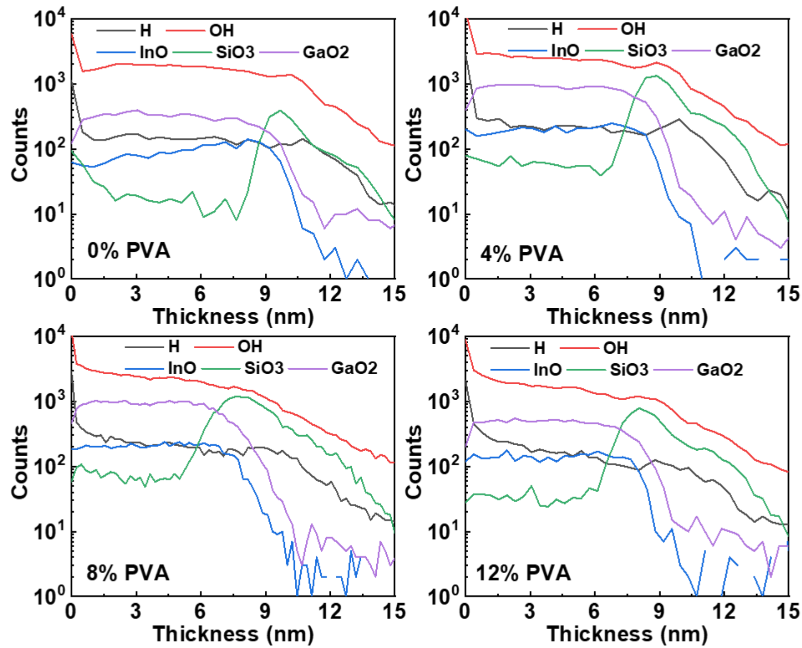

Figure S17. ToF-SIMS depth profile of the IGO:PVA films fabricated on Si wafers.

9. IGO:PVA powders and the corresponding SS-NMR measurements

Note that the fabrication process for the IGO:PVA powder samples was by drop-casting the blend precursors on Si wafers and annealing at 300 ºC for multiple cycles. The resulting powders show identical chemical compositions and also an amorphous microstructure by GIXRD (Table S10 and Figure S18).

Table S10. Atomic percentage of In, Ga, O, and C in IGO:PVA powders with different PVA contents (T_{anneal} = 300 ºC).

PVA content (wt.%)	0	4	8	12
In (at.%)	24.1	25.0	23.9	23.4
Ga (at.%)	17.3	17.4	17.4	17.1
O (at.%)	55.7	55.0	55.4	55.8
C (at.%)	2.9	2.7	3.3	3.7

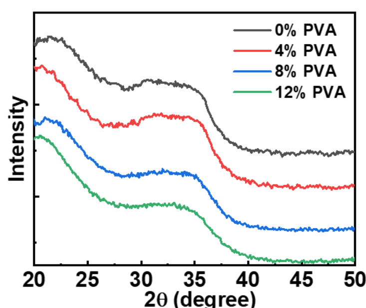

Figure S18. Powder XRD for IGO:PVA powders with different PVA contents.

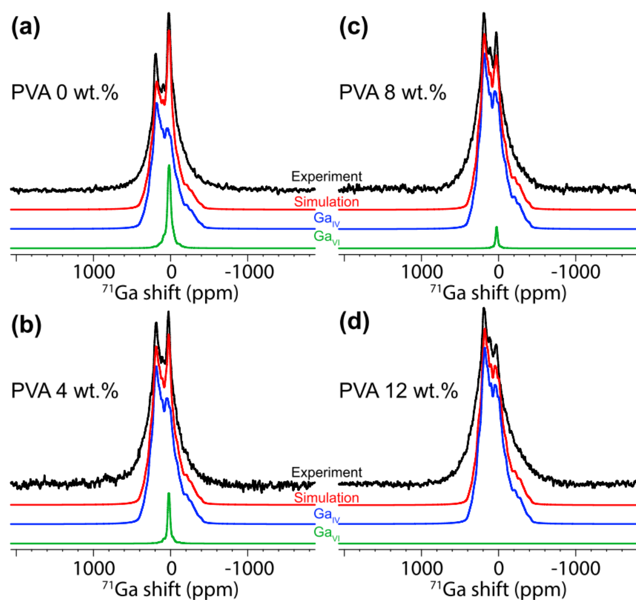

Figure S19. ^{71}Ga MAS NMR spectra of IGO:PVA powders.

Table S11. [71]Ga NMR simulation results for four IGO:PVA powders, where η is the deviation from axial symmetry of the electric field gradient tensor

wt.% PVA in IGO	Parameters	Components	
		Ga_{IV}	Ga_{VI}
0	Shift (ppm)	212	41
	C_Q (MHz)[a]	19.7	7.7
	η	1	0.082
	Fraction (%)	86.2	13.8
4	Shift (ppm)	216	39.7
	C_Q (MHz)[a]	19.7	6.9
	η	1	0.035
	Fraction (%)	94.8	5.2
8	Shift (ppm)	216	38.6
	C_Q (MHz)[a]	19.7	5.8
	η	1	0.015
	Fraction (%)	98.2	1.3
12	Shift (ppm)	215	N/A
	C_Q (MHz)[a]	19.9	N/A
	η	1	N/A
	Fraction (%)	100	0

[a] Considering only the central transition.

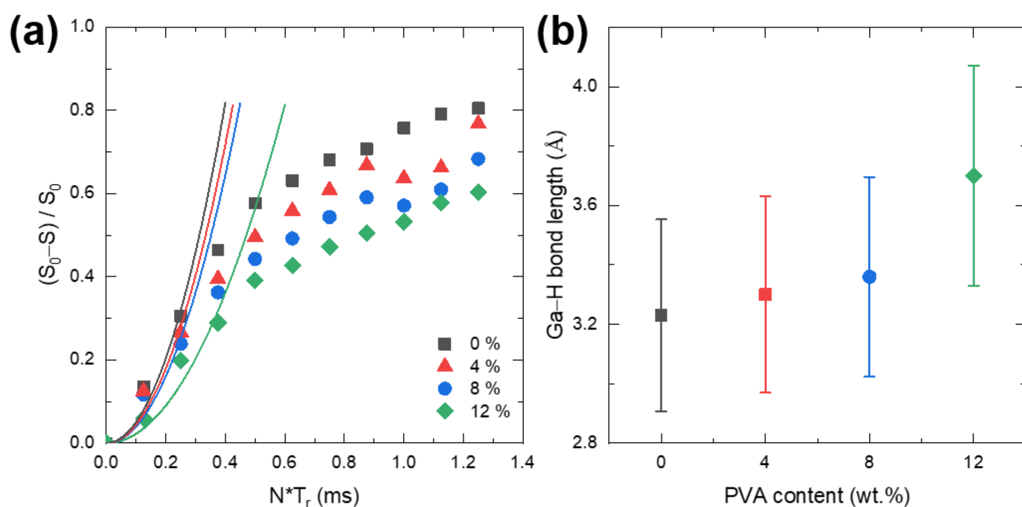

Figure S20. (a) The [71]Ga{[1]H} REDOR plots and the associated fitting of the indicated IGO:PVA powders. (b) The fitted Ga-H bond length in IGO:PVA powders based different PVA incorporations. Due to the imperfect 180° pulses that could affect the effectiveness of dipolar recoupling, and limited data range for fitting to exclude the impact of coupling scheme of multiple nuclei pairs, about 10% of errors are obtained.

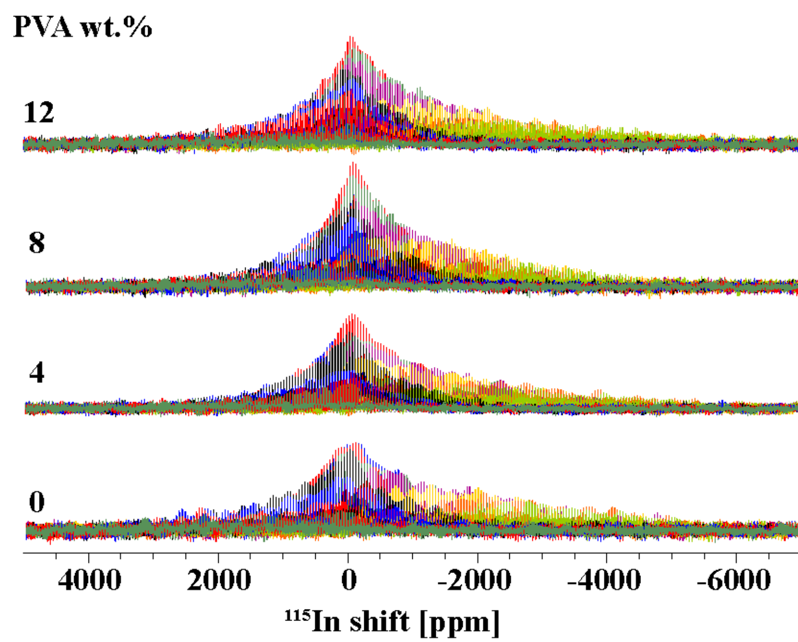

Figure S21. ^{115}In MAS NMR spectra of IGO:PVA powders.

10. Theoretical Calculations on IGO with hydrogen doping

Details of theoretical approach

The amorphous $In_{32}Ga_{22}O_{80}$ and $In_{32}Ga_{22}O_{79}$ structures (In:Ga ≈ 6:4) were obtained using *ab-initio* molecular dynamics (MD) liquid-quench approach as implemented in the Vienna Ab Initio Simulation Package (VASP) (32-35). The calculations are based on the density functional theory (DFT) (36, 37) with periodic boundary conditions and employ PBE functional (38, 39) within the projector augmented-wave method (40, 41). A bixbyite cell of In_2O_3 with 134 atoms per cell was used as initial structure which was melted at 3,000 K to eliminate any crystalline memory. For amorphous Ga-doped indium oxide, random In atoms were substituted with Ga atoms with In/Ga ratio of 1.455, and the $In_{32}Ga_{22}O_{80}$ cell density was adjusted to 6.71 gm/cm^3. The latter was calculated based on the crystalline density of 7.12 gm/cm^3 for In_2O_3 and the fraction of Ga_2O_3 having the crystalline density of 6.44 gm/cm^3; the resulting density was then reduced by about 3% to represent an amorphous case. To model non-stoichiometric structures with lower oxygen content, oxygen atom(s) were randomly removed. All structures had additional melting at 3,000 K for at least 10 ps in order to randomize the sub-stoichiometric multicomponent configuration and stabilize the total energy. Next, liquid quench simulations were performed as follows. Each structure was cooled to 2,500 K at the MD rate of 100 K/ps and then rapidly quenched to 100 K at 200 K/ps rate. An energy cut-off of 260 eV and single Γ-point were used during melting and quenching processes. Finally, each structure was equilibrated at 300 K for 6 ps with a cut-off energy of 400 eV. All MD simulations were carried out in the NVT ensemble with the Nose-Hoover thermostat using an integration time step of 2 fs. For an accurate structural analysis of the simulated amorphous oxides, the room-temperature In-Ga-O structures were used. The average pair correlation function and the average effective coordination number were calculated according to Refs. (42-44). The resulting atomic structures were plotted using VESTA software (45). Next, the atomic configurations obtained from the *ab-initio* MD simulations were optimized within DFT using the PBE functional. For the optimization, the cut-off energy of 500 eV and the 4x4x4 Γ-centered k-point mesh were used; the atomic positions were relaxed until the Hellmann-Feynman force on each atom was below 0.01 eV/Å.

To determine the structural preferences of hydrogen in the amorphous indium-gallium oxide, to understand the importance of Ga doping, and to calculate the resulting electronic properties of H-doped a-In-Ga-O, twenty structurally unique interstitial positions for a single Hydrogen atom were selected out of about 50 possible interstitial H locations with the distance between the H atom and its nearest neighbor atom (oxygen or metal) of at least 1.65 Å in each amorphous $In_{32}Ga_{22}O_{80}$ and $In_{32}Ga_{22}O_{79}$ structures. This can be compared to the In-H distance of 1.68 Å in InH_3 or the typical O-H distance of 1.0 Å. The longest distance between the initial H position and its nearest neighbor was 2.05 Å, corresponding to the largest interstitial space in our amorphous structure. The 40 structurally unique H locations in $In_{32}Ga_{22}O_{80}$ and $In_{32}Ga_{22}O_{79}$ structures represent different nearest-neighbor environment for the interstitial H, with different number of In and/or Ga neighbors and different coordination for the neighboring metal or oxygen atoms. The results allowed us to determine the energetically most preferable H position once the H-doped structures were fully re-optimized within DFT. Specifically, the local structure in the vicinity of the interstitial H atom in each case, including bond lengths, effective coordination of neighboring M and O atoms, and degree of the local distortions in the M-O polyhedra before and after H doping were carefully studied and compared based on the calculated total energy of the fully relaxed structures.

The electronic and optical properties of the DFT-optimized amorphous H-free and H-doped In-Ga-O structures were calculated using the hybrid Heyd-Scuseria-Ernzerhof (HSE) approach (46, 47) with a mixing parameter of 0.25 and a screening parameter α of 0.2 Å^{-1}. To characterize the localization of the electronic states within the band gap and near the band edges, the inverse participation ratio (IPR) was calculated. IPR calculations help quantify the electron localization: the higher the IPR value, the stronger the localization is; *vice versa*, a delocalized state corresponds to a value of 1. Optical absorption was derived from the frequency-dependent dielectric function, $\varepsilon(\omega) = \varepsilon_1(\omega) + i\varepsilon_2(\omega)$, calculated within independent particle approximation as implemented in VASP. The imaginary part, $\varepsilon_2(\omega)$, is related to the optical absorption at a given frequency ω, and is determined based on the electronic transitions of the hybrid functional solution. The real part of the complex dielectric function is obtained using Kramers-Kronig relations.

The defect formation energies were calculated based on the total energies obtained for fully-relaxed structures from HSE calculations according to the following equation:

$$\Delta E_{\text{formation}}(\mu_C) = E(\text{IGO:H}) - [E(\text{IGO}) + \mu_C(\text{H})],$$

where μ_C is the hydrogen chemical potential calculated based on the half of the total energy of H_2 molecule.

Discussion of the Theoretical Analysis of IGO Hydrogen Doping

It is important to stress here that while the structure and electronic properties of H-doped crystalline In_2O_3 have been investigated, (48, 49) the H bonding strength and thermal stability as well as the resulting properties are expected to be different in H-doped amorphous oxides. Strong local distortions in the metal-oxygen (M-O) polyhedra are expected to favor the formation of H defects, whereas the disorder in an M-O polyhedral network (i.e., the lack of symmetry-specific crystallographic sites and periodicity) is likely to promote H diffusion. Furthermore, because our experimental data demonstrate that Ga-containing matrices behave very differently with PVA doping than does In_2O_3 (*vide infra*, Figure 6a), and also that deep traps are affected, amorphous oxides with an In:Ga ratio of 6:4 and with different oxygen stoichiometries were analyzed theoretically.

The results suggest that the most energetically favorable configurations in both $In_{32}Ga_{22}O_{80}H_1$ and $In_{32}Ga_{22}O_{79}H_1$ correspond to the formation of M-OH units with H-O bond lengths of ≈1.0 Å (Figure 5a). This represents a strong covalent OH^- bond as confirmed by the calculated Bader charge transfer (Figure 5a, below) and by the reduced effective coordination number (ECN) of the oxygen atom that decreases from 2.0 (2.3) in H-free structures to 1.2 (1.8) after bonding to H in $In_{32}Ga_{22}O_{80}H_1$ (in $In_{32}Ga_{22}O_{79}H_1$). Accordingly, the distances between this oxygen and its nearest M neighbors increase from 1.81 Å, 2.09 Å, and 2.18 Å for Ga, In, and another In neighbor before H-doping to 1.89 Å, 2.21 Å, and 2.46 Å, respectively, after the M-OH formation in $In_{32}Ga_{22}O_{80}H_1$. The changes are similar in $In_{32}Ga_{22}O_{79}H_1$, where H bonds to an oxygen with two Ga neighbors, enlarge the Ga-O distances from 1.82 Å and 1.89 Å before H-doping to 1.88 Å and 1.96 Å, respectively, after the OH formation. In both cases, the OH formation weakens the metal-oxygen bonds in the M-OH complex. Note, that the M-OH structure in amorphous IGO is similar to the one found in H-doped crystalline In_2O_3 with an O-H distance of 1.0 Å and an increased In-O distances upon H doping (from 2.20 Å to 2.31 Å, on average), although the initial coordination of the oxygen atoms (4.0) is large in crystalline In_2O_3.(48, 49)

To understand the importance of the Ga presence in the In-based oxide, the local structure of H-doped IGO was analyzed further. First of all, although nearly half of the 40 initial H locations in IGO have In atoms among its nearest neighbors, and the lowest energy configurations after the relaxation always have at least one Ga bonded to the OH group. Moreover, in both $In_{32}Ga_{22}O_{80}H_1$ and $In_{32}Ga_{22}O_{79}H_1$, the most stable Ga-OH configuration corresponds to the shortest Ga-O bond length, 1.81 Å (1.82 Å), and to the lowest ECN for both O and Ga among their atom types, namely, 2.00 (2.26) for O and 3.72 (3.84) for Ga atom in the initial $In_{32}Ga_{22}O_{80}$ ($In_{32}Ga_{22}O_{79}$) structures, *i.e.*, before H addition. For comparison, the average Ga-O distance is 2.01 Å (1.97 Å) and the average ECN of O and Ga atoms are 3.08 (2.90) and 4.84 (4.63), respectively, in DFT-optimized H-free $In_{32}Ga_{22}O_{80}$ ($In_{32}Ga_{22}O_{79}$). Upon H-doping, in addition to the aforementioned increase of the Ga-O distances, we find that the formation of M-OH reduces the local distortions in all neighboring MO polyhedra from 3.18×10^{-2} Å^2 to 1.60×10^{-2} Å^2 (from 2.86×10^{-2} Å^2 to as low as 4.08×10^{-3} Å^2) for the nearest M neighbors of the oxygen atom bonded to H in $In_{32}Ga_{22}O_{80}H_1$ ($In_{32}Ga_{22}O_{79}H_1$). As shown below, the decreased M-O distortions and the associated weakening of the strongest Ga-O bonds upon the OH^- formation, result in significantly higher contributions from these metal atoms to the conduction band states near the Fermi level, improving free carrier transport. This finding helps explain the mobility increase observed experimentally upon PVA doping: the fraction of 4-coordinated Ga is found to increase with increasing PVA content (Table S11), because the abundance of severely under-coordinated Ga and O with short Ga-O bonds attracts hydrogen that helps reduce the local distortions, enhancing the mobility.

Furthermore, the presence of low-coordinated oxygen atoms (that attract H) is attributed to the Ga doping. Indeed, the fraction of O atoms with ECN < 2.80 increases from 4 % in undoped a-IO to 31 % in a-IGO even at low In:Ga ratio of 4:1. This is the largest fraction among the post-transition metal dopants, including Sn (with an under-coordinated oxygen fraction of 17 %) or Zn (with 11 %), in amorphous indium oxide having the same In:X ratio.(19) This finding is in accord with the lowest O coordination in monoclinic Ga_2O_3 (ECN=2.32, 2.84, and 3.39 for three O types), followed by rutile SnO_2 (ECN = 2.96), whereas all oxygen atoms are 4-coordinated in crystalline In_2O_3 and ZnO.(19) Hence, among the post-transition metal dopants in amorphous indium oxide, Ga is likely to provide the best environment to benefit from the H presence. Note that at a high In:Ga ratio of 6:4, the number of the low-coordinate oxygen atoms (ECN < 2.80) continues to rise to 37 % for $In_{32}Ga_{22}O_{80}$ and reaches 50 % in $In_{32}Ga_{22}O_{79}$ (Figure S22a).

In addition, we find that formation of the OH bond results in a different effect on the Ga and In coordination with oxygen: the average Ga coordination slightly increases, from 4.63 to 4.65, whereas the average In coordination significantly decreases, from 5.33 to 5.24, as found in the fully-relaxed structures before and after H-doping, respectively. Importantly, the presence of H may affect the coordination of atoms that are located further away from H than its first, second, or third nearest neighbors – likely, due to the long-range bond reconfiguration that was found to occur in the amorphous indium oxide structure.(50)

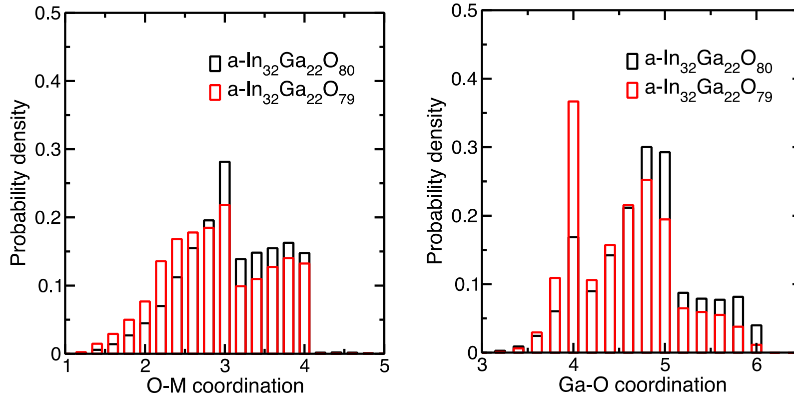

Figure S22. The calculated effective coordination number distributions in H-free amorphous $In_{32}Ga_{22}O_{80}$ and $In_{32}Ga_{22}O_{79}$ for (a) O-M and (b) Ga-O. The results are obtained from MD simulations at room temperature.

Among the 40 cases considered here with various initial H locations in $In_{32}Ga_{22}O_{80}H_1$ and $In_{32}Ga_{22}O_{79}H_1$, the higher-energy (less-favorable) configurations correspond to the formation of interstitial H with the average distances to Ga or In atoms of 1.65 Å or 1.83 Å, respectively. These distances are longer than the corresponding distances in GaH_3 (1.48 Å) and InH_3 (1.68 Å);(51) yet, they are significantly shorter than those in H-doped crystalline In_2O_3 (2.13 Å)(48, 49) – as expected from the much stronger M-O distortions in the amorphous oxide. The calculated Bader charge for H is 2 e^- which means that the H radical gains an additional electron once in the lattice to becomes H^-. The H receives the charge from the nearest neighboring metals – as illustrated by the calculated charge transfer, Figure 5b. It is important to note here that our *ab-initio* MD simulations at room temperature (see below) show that the interstitial H may become stable only in highly sub-stoichiometric oxides ($IGO_{2.92}$), i.e., when a large number of metal atoms that are severely under-coordinated and highly distorted, begin to cluster with each other, attracting H. Indeed, the calculated defect formation energy, 0.35 eV for most favorable M-OH and 0.56 eV for most favorable interstitial H in $In_{32}Ga_{22}O_{80}H_1$ decreases to –0.08 eV for most favorable M-OH and 0.01 eV for most favorable interstitial H in $In_{32}Ga_{22}O_{79}H_1$, suggesting that the room-temperature concentration of H interstitial is about 7 orders of magnitude lower than that of OH^-in nearly-stoichiometric $IGO_{2.96}$, while it becomes 3 orders of magnitude lower than that of OH in highly O-deficient $IGO_{2.92}$.

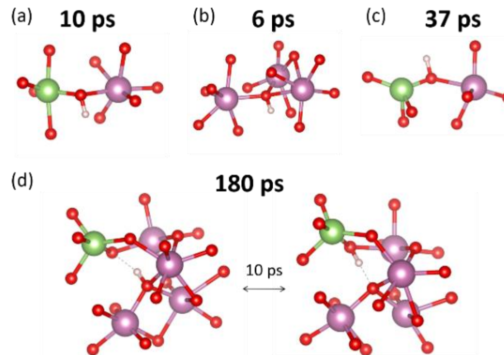

Figure S23. The local M-OH structures obtained during room temperature MD simulations for $In_{32}Ga_{22}O_{80}H_1$. In the configuration shown, the OH complex is stable (i.e., the O-H distance remains close to 1 Å) for (a) 10 ps; (b) 6 ps; and (c) 37 ps. Then, H spends 180 ps being shared between two oxygen atoms, forming an OH bond with each of the oxygen atoms for less than 10ps before switching to the other one (d).

In $In_{32}Ga_{22}O_{80}H_1$ with a higher oxygen stoichiometry (2.96) and smaller fraction of 4-coordinated Ga (40%), H spends 10 ps at its initial (most favorable at 0 K) position bonded to an oxygen atom with the lowest initial ECN= 2.0 (Figure S23a); then it travels extensively throughout the cell, Figure 5c, bonding to an oxygen atom with initial ECN= 3.7 for 6 ps (Figure S23b) and then with another oxygen atom with initial ECN=2.4 for 37 ps (Figure S23c); and finally, it becomes trapped for more than 180 ps between two oxygen atoms (Figure S23d, initial ECN= 2.8 and 3.7), making an OH^- bond with each of the O atoms for less than 10 ps intervals before switching to the other O, Figure S24a.

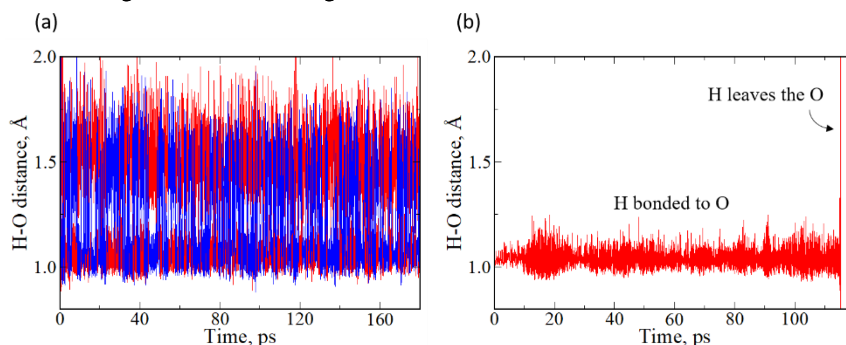

Figure S24. The calculated distances between Hydrogen and Oxygen atoms in (a) unstable O-H bonding where the H switches between two Oxygen atoms with the O-H distances shown in red and blue for different O atoms, and (b) stable O-H bond where H remains to be bonded to the same O atom. The results are obtained from MD simulations at 300 K with 2 fs time step.

In striking contrast to the $In_{32}Ga_{22}O_{80}H_1$ case above, H spends more than 11 times longer (115 ps) bonded to the oxygen atom with the lowest ECN when room-temperature MD simulations are initiated using the most stable 0K DFT position in $In_{32}Ga_{22}O_{79}H_1$ (Figures 5d and S25a). During this time period, the calculated O-H distance varies insignificantly due to thermal fluctuations, representing a stable covalent O-H bond, Figure S24b. We believe that the stronger OH^- bonding occurs because the oxygen atom in this case has two Ga neighbors, and both Ga-O distances are the shortest in the corresponding Ga polyhedra, creating a deeper potential well and, thus, making it harder for H to escape. This finding explains the observed OH^- bond strengthening with increasing PVA content: since the fraction of 4-coordinated Ga atoms increases with PVA doping, Table S11, the probability for highly-distorted GaO_4 polyhedra to connect through an under-coordinated O via shortest Ga-O bonds, trapping H for longer times increases as well. After 115 ps, the H escapes and travels a short distance to be shared as an interstitial between two under-coordinated In atoms (Figure S25b, ECN= 4.7 and 5.4) for about 6 ps; and then it becomes trapped between highly-distorted Ga and In atoms (ECN=3.7 and 4.7, respectively) for 127 ps (Figure S25c).

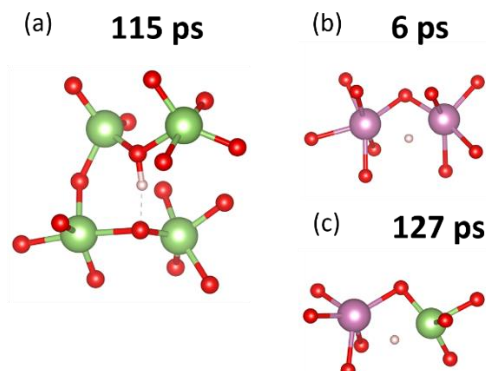

Figure S25. The local M-OH structures obtained during room temperature MD simulations for $In_{32}Ga_{22}O_{79}H_1$. In the configuration shown, the OH complex is stable (i.e., the O-H distance remains close to 1 Å) for (a) 115 ps; then H becomes an interstitial for (b) 6 ps and (c) 127 ps.

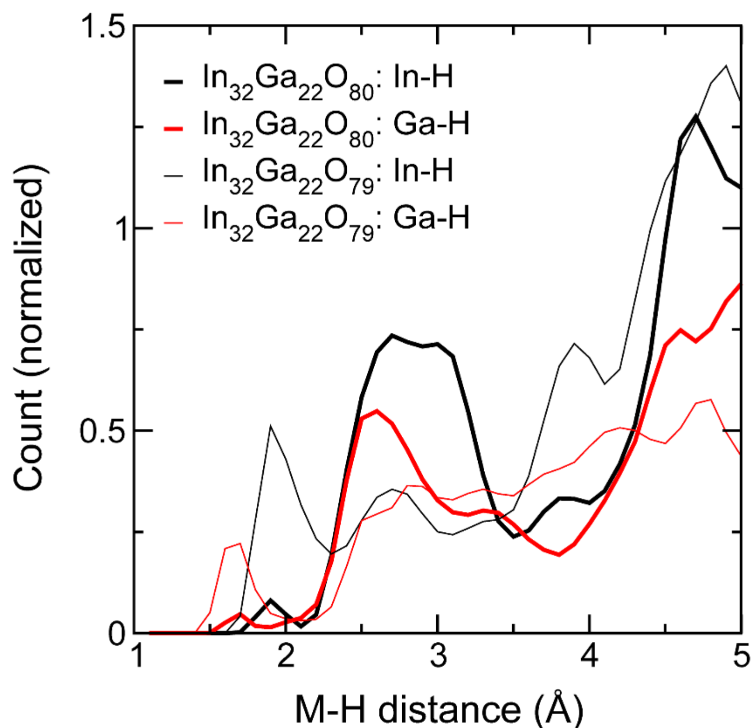

Figure S26. M-H distance distributions calculated from ab-initio MD at 300K. The results are an average of 20 configurations for each stoichiometry ($IGO_{2.96}$ and $IGO_{2.93}$) and also a time average of ~180 ps (~100,000 MD steps) in each case (a total of 3.6M configurations were analyzed).

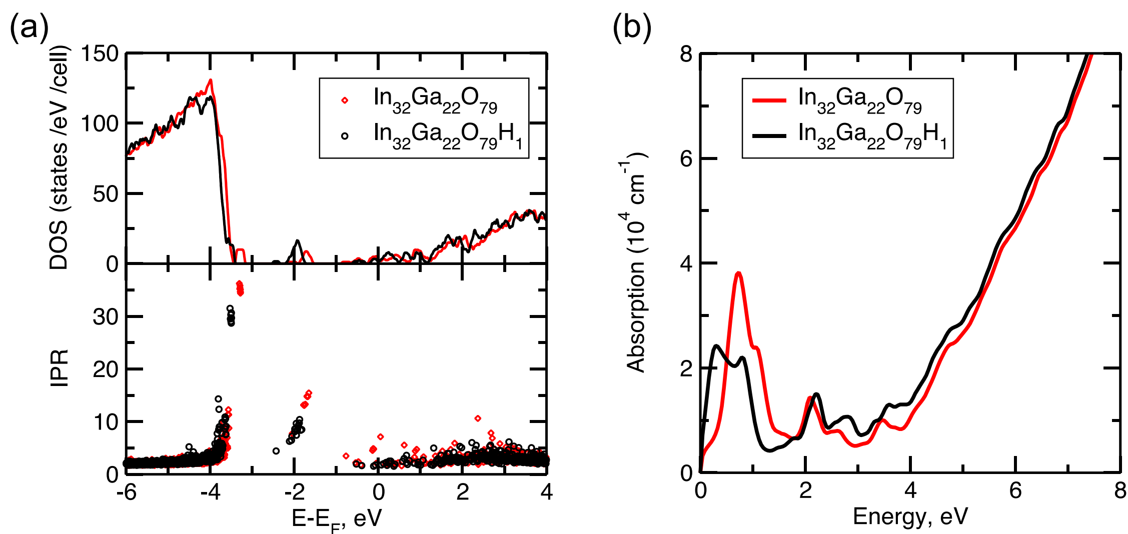

Figure S27. (a) Calculated density of states (DOS) and inverse participation ratio (IPR) and (b) optical absorption for $In_{32}Ga_{22}O_{79}$ and $In_{32}Ga_{22}O_{79}H_1$ as obtained from DFT-HSE calculations.

11. Role of Ga and PVA in IGO:PVA films

11.1. In_2O_3:PVA and IZO:PVA films

Previously, we reported that PVA suppresses charge transport in In_2O_3:PVA TFTs from ≈ 4 cm^2/Vs (pristine In_2O_3) to ≈ 0.6 cm^2/Vs with 6% wt. PVA in the MO precursor solution (Figures 6 and S28).(30) Here, IZO:PVA and IGZO:PVA films were also fabricated to further probe the mechanism of PVA incorporation in IGO. As shown in Figure S29, in IZO:PVA (In:Zn = 7:3) TFTs, I_{ON} monotonously decreases from 1.79×10^{-3} A to 1.20×10^{-7} A to 4.91×10^{-4} A, and to 1.58×10^{-4} A, as the PVA content increases from 0 wt.% to 1 wt.%, 4 wt.% and 8 wt.%, respectively, decreasing the electron mobility and shifting V_T to more positive values (Figure 6b).

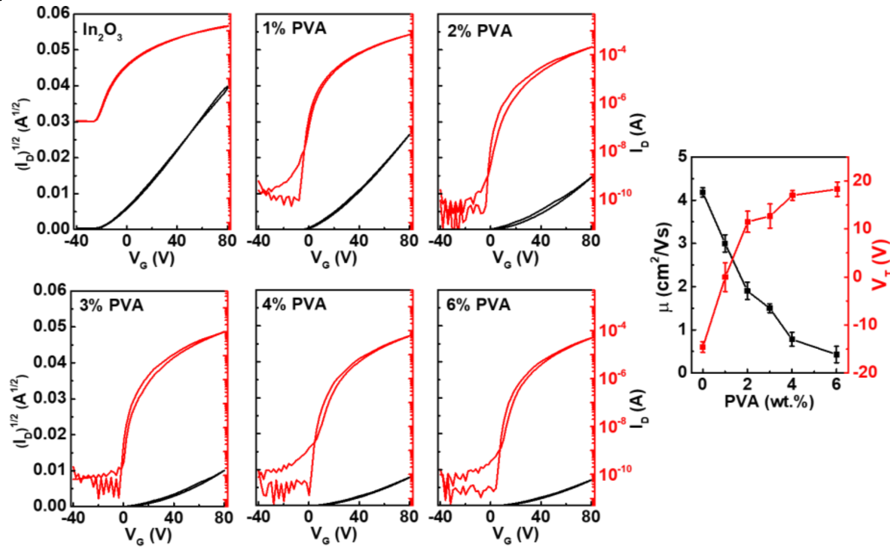

Figure S28. Representative experimental transfer curves for TFTs based on In_2O_3:PVA films with different PVA content (V_D = +80 V, annealing temperature 250 ºC), along with calculated mobility and V_T of In_2O_3 TFTs with different PVA content.(30)

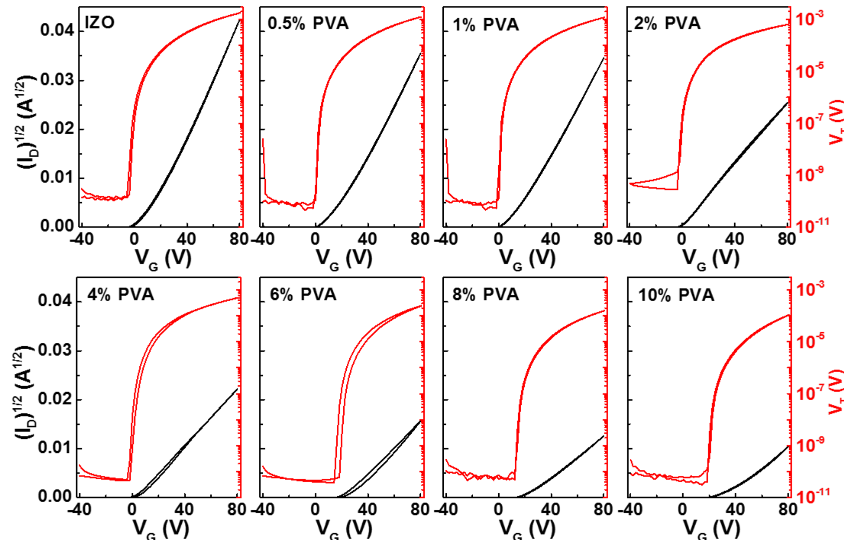

Figure S29. Representative experimental transfer curves for TFTs based on IZO:PVA films with different PVA contents (V_D = +80 V, annealing temperature 300 ºC).

Note that AFM analysis of IZO:PVA films (Figure S30) indicates that all films are equally smooth suggesting that the poorer TFT performance with PVA incorporation is not attributable to deterioration of film topology. However, O 1s XPS analysis of IZO (Figure S31) reveals that upon PVA incorporation, the M-O-M content

gradually decreases from 71.9 % (0 wt.% PVA) to 67.8% (4 wt.% PVA) to 62.4% (8 wt.% PVA) and then to 59.9% (12 wt.% PVA), a very different trend than observed for the IGO:PVA films where it always remains > 70% (Figure 1c) due to the strong "oxygen getter" effects of Ga.(52)

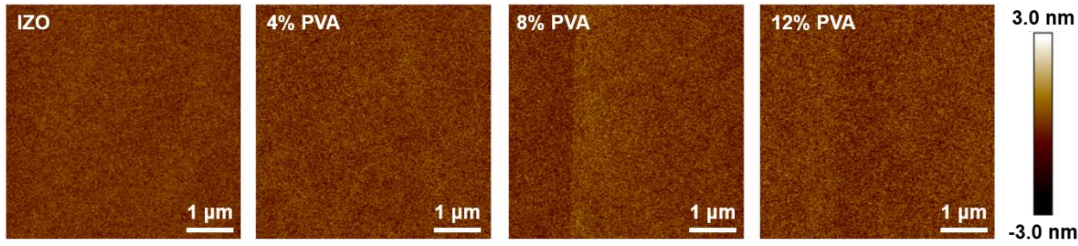

Figure S30. AFM images for IZO-PVA films with different PVA content. The RMS roughness is less than 0.3 nm.

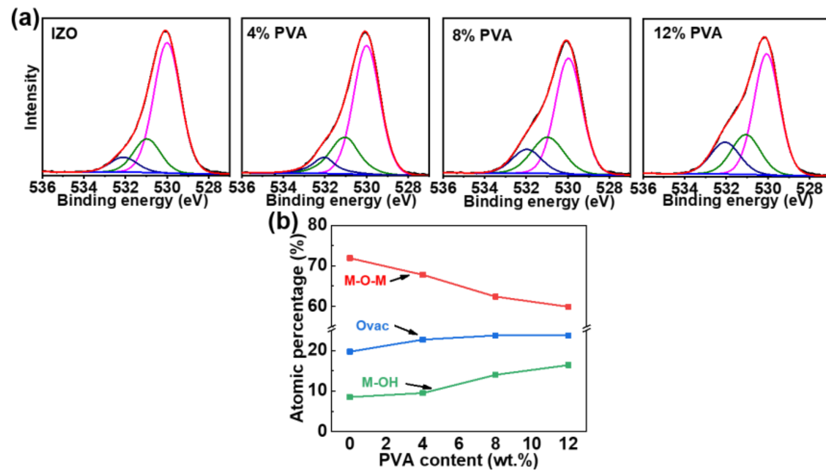

Figure S31. (a) XPS O 1s for IZO:PVA films with different PVA contents. (b) Summary of the relative M-O-M, O_{vac}, and M-OH contents by fitting the IZO:PVA film XPS O 1s peaks.

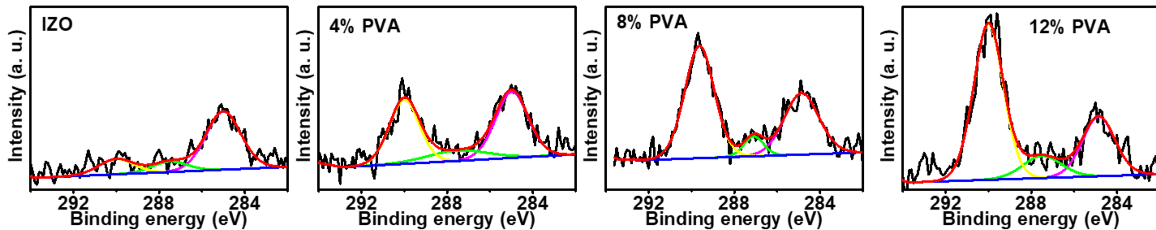

Figure S32. XPS C 1s spectra for IZO:PVA films with different PVA contents.

11.2 IGZO:PVA films

To further probe the impact of PVA introduction OM films with different cations, IGZO:PVA films with two different metal compositions (In:Ga:Zn = 72.5:7.5:20 and 1:1:1) were fabricated and characterized in TFT geometries (Figures S33 and S34). As shown in Figure 6, while the mobility of IGZO(72.5:7.5:20) TFTs always decreases with increasing the PVA content [from 4.44±0.37 cm^2/Vs (0 wt.% PVA) to 2.65±0.23 cm^2/Vs (2 wt.% PVA) to 2.23±0.20 cm^2/Vs (6 wt.% PVA)], for IGZO(1:1:1) the mobility first increases steeply from less than 10^{-3} cm^2/Vs (0 wt.% PVA) to ≈0.086 cm^2/Vs (4 wt.% to 8 wt.% PVA) and only then decreases. It is obvious that for the IGZO with less Ga (IGZO with In:Ga:Zn = 72.5:7.5:20), PVA does not promote carrier mobility and only enlarges V_T (Figure 6) in contrast to the Ga-rich (In:Ga:Zn = 1:1:1) composition in which the mobility increases and V_T is reduced (Figure 6).

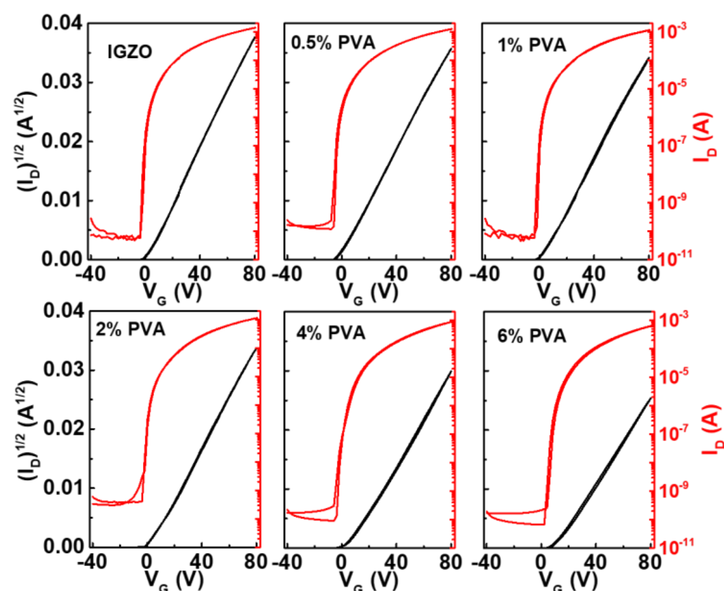

Figure S33. Representative transfer curves for TFTs based on IGZO (72.5:7.5:20) with different PVA contents (V_D = +80 V, annealing temperature 300 °C).

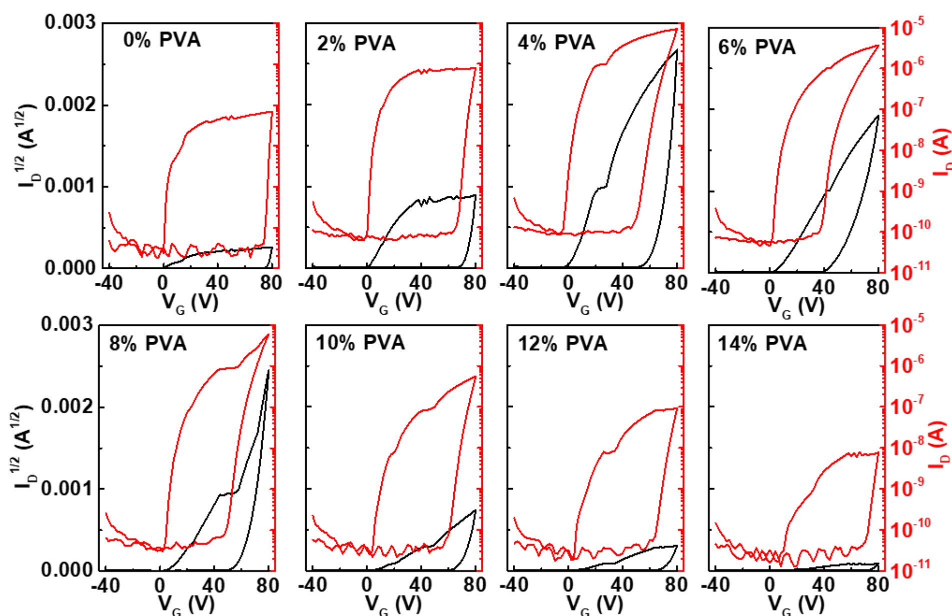

Figure S34. Representative transfer curves for TFTs based on IGZO (1:1:1) with different PVA contents (V_D = +80 V, annealing temperature 300 °C).

11.3 IGO:PVP films

Precursor preparation. 354.8 mg of $In(NO_3)_3 \cdot xH_2O$, 399.6 mg of $Ga(NO_3)_3 \cdot xH_2O$ were dissolved in 20 mL 2-methoxythenol, respectively. After the metal nitrates were completely dissolved, the solutions were mixed to obtain a In/Ga molar ratio of 6/4. PVP was dissolved in 2-methoxythenol to yield a concentration of 20 mg/mL. Then, PVP was added to the IGO precursor solution to yield compositions of polymer:metal oxide ranging from 0% to 12% in weight of PVA.

PVA plays a critical role in optimizing the H bonding configuration, lowering the formation energy and strengthening O-H bonding (Figure 5). Consequently, the decreased distortions in the MO polyhedra not only

contribute to more uniform conduction states, but also reduce deep defect localization. Note also that, compared with our previous work on other MO-polymer systems such as using PEI and PVP,(27, 30) PVA contrasts in two important aspects: 1). No electron-rich electron donor groups (vs. amino groups in PEI) are present; 2). Compared to PVP, PVA cleanly decomposes during the fabrication process. Interestingly, PVA is effective in enhancing transport only for metal oxides with a relatively large Ga content, since only with substantial Ga content can high M-O-M densities be preserved on PVA incorporation. This is further supported by the weak decrease on electron density when incorporating PVA [from 1.42 e/ $Å^3$ (0 wt.% PVA) to 1.39 e/ $Å^3$ (8 wt.% PVA), Table S8]. Furthermore, since IGO:PVP films always yield inferior TFT (Figures 6, and S35) performance due to largely remained polymer content in IGO-PVP films (Figure S36), it is clear that realization of high-performance Ga-rich MO oxide semiconductors requires the use of a thermally labile polymer.

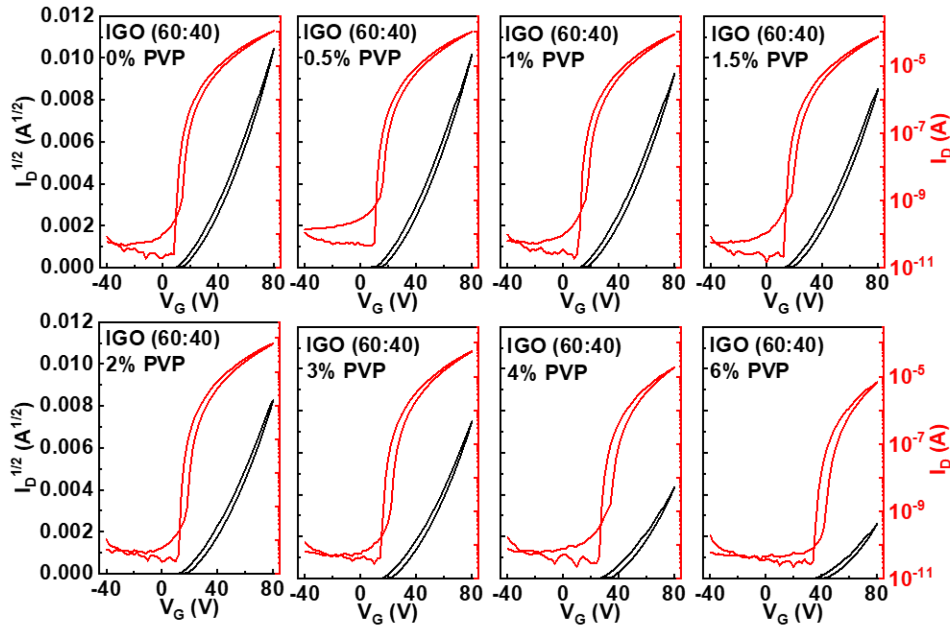

Figure S35. Representative transfer curves for TFTs based on IGO (60:40) with different PVP contents (V_D = +80 V, annealing temperature 300 ºC).

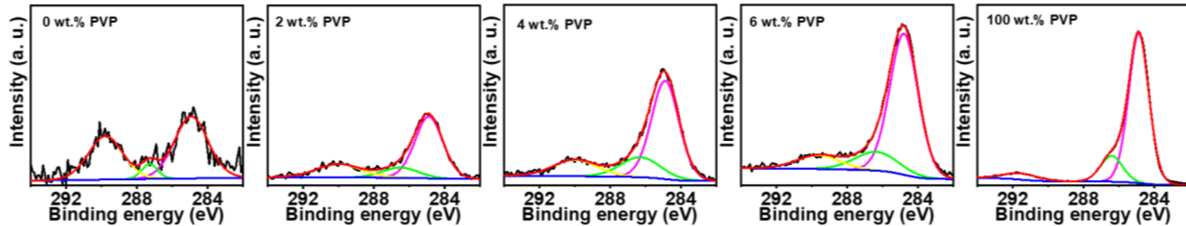

Figure S36. XPS C 1s of PVP and IGO-PVP films with different PVP contents.

11.4 IGO:Glycerol films

Glycerol (Gly, a small poly-hydroxy molecule) was next investigated to replace PVA as a dopant since it shares similar chemical structures with large densities of -OH functional groups and Gly decomposes easier compared to PVA (infra versa, Figure S37). As shown in Figure S37, similar to PVA-doped IGO, a very large increase in I_{ON} is obtained along with reduced hysteresis when Gly is added to the precursor. The TFT mobility and V_T (Figure 6) also indicate that glycerol incorporation enhances device performance, with an increased mobility of 0.91 cm^2/Vs (4 wt.% Gly), and 0.56 cm^2/Vs (8 wt.% Gly). Additionally, TGA/DSC measurements on the dried precursors, IGO-0 wt.% PVA, IGO-8 wt.% PVA, and IGO-8 wt.% Gly (Figure

S38), indicate that all the precursors exhibit endothermic behavior, excluding the possibility that the performance enhancement is due in any large extent to combustion synthesis,(53, 54) and thus differences in heat evolution during the exothermic conversion to MOs. Moreover, since glycerol is a small molecule with functional groups (-OH) similar to those of PVA, it should act similarly to PVA, and leave less residue in the resulting IGO films. Nevertheless, for PVA incorporation, a champion mobility of >7 cm^2/Vs is obtained, which is 7x times higher than with Gly incorporation. We suspect that the exceptionally high mobility for low-temperature solution processed IGO (In:Ga = 6:4) films with PVA incorporation is due to the following factors. As shown in the TGA plots of Figure S39 PVA thermolysis process is very different than that of Gly, with the latter compound being completely decomposed/vaporized below 200 ºC while PVA begins decomposition at ≈250 ºC with the majority of the weight loss only occurring at ≈300 ºC. Note, however that PVA decomposition is far more efficient than that of PVP; see Figure S36, where large amounts of PVP remain in the oxide film. As a result, the relatively slow decomposition speed of PVA may act as an additional shield that facilitates hydrogen diffusion to energetically stable sites in IGO, since the majority of the hydrogen in the films originate from the annealing atmosphere (Figure S13). Moreover, the PVA decomposition process may also generate oxygen vacancy densities and, stronger O-H bonding, supported by both experimental and simulation results.

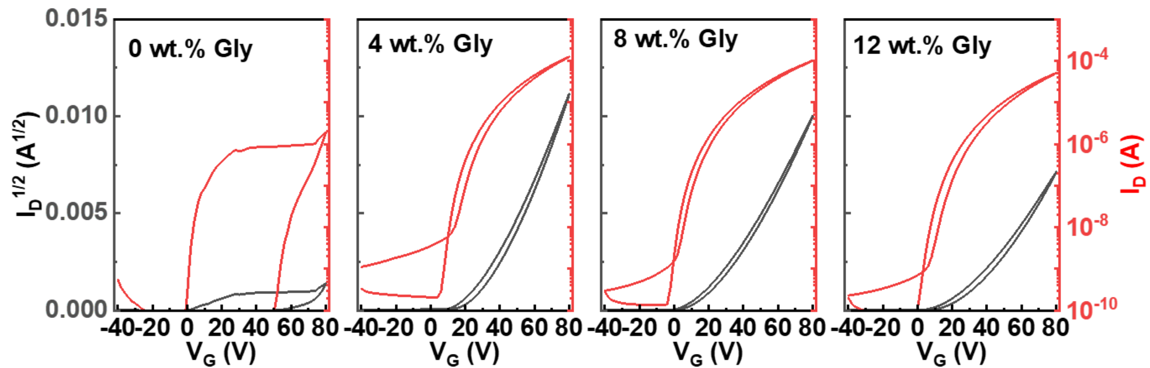

Figure S37. Representative transfer curves of TFTs based on IGO (60:40) with different glycerol content (V_D = +80 V, annealing temperature 300 ºC). Note, the glycerol was first dissolved in DI water with a concentration of 16 mg/ml, other than that, the rest of the process is identical to that of IGO:PVA based transistors.

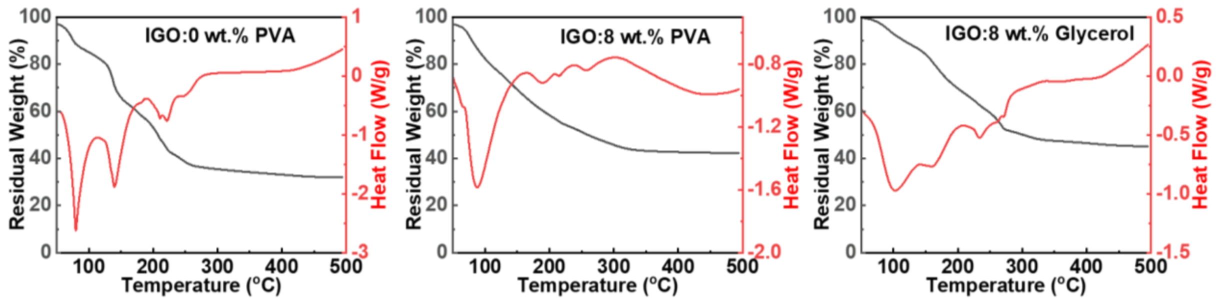

Figure S38. TGA-DSC curves of dried precursor of IGO:0 wt% PVA, IGO:8 wt.% PVA, and IGO:8 wt.% Gly.

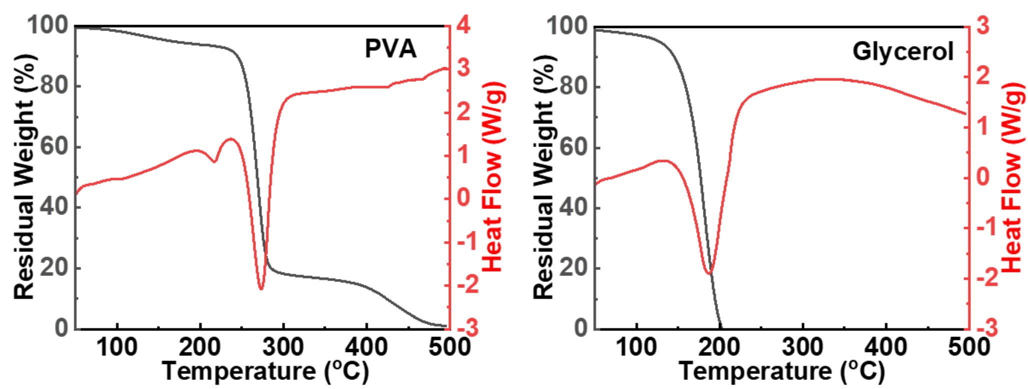

Figure S39. TGA-DSC curves of pure PVA and Glycerol.

SI References

1. Z. Zhu*, et al.*, Polymer-Doped Ink System for Threshold Voltage Modulation in Printed Metal Oxide Thin Film Transistors. *J Phys. Chem. Lett.*, 3415-3419 (2019).
2. H. Young Hwan, B. Byeong-Soo, Effect of Aluminum and Gallium Doping on the Performance of Solution-Processed Indium Oxide Thin-Film Transistors. *J. Disp. Technol.* 9, 704-709 (2013).
3. F. Shao, Q. Wan, Recent progress on jet printing of oxide-based thin film transistors. *J. Phys. D: Appl. Phys.* 52, 143002 (2019).
4. K. K. Banger*, et al.*, Low-temperature, high-performance solution-processed metal oxide thin-film transistors formed by a 'sol-gel on chip' process. *Nat. Mater.* 10, 45-50 (2011).
5. J. H. Park, Y. G. Kim, S. Yoon, S. Hong, H. J. Kim, Simple method to enhance positive bias stress stability of In-Ga-Zn-O thin-film transistors using a vertically graded oxygen-vacancy active layer. *ACS Appl. Mater. Interfaces* 6, 21363-21368 (2014).
6. R. Sanjinés*, et al.*, Photoemission spectromicroscopy: A new insight in the chemistry of SnOxfilms for gas sensors. *J Appl. Phys.* 73, 3997-4003 (1993).
7. S. Kačiulis, G. Mattogno, A. Galdikas, A. Mironas, A. Šetkus, Influence of surface oxygen on chemoresistance of tin oxide film. *J. Vac. Sci. Technol., A* 14, 3164-3168 (1996).
8. T. Ishida, H. Kobayashi, Y. Nakato, Structures and properties of electron‐beam‐evaporated indium tin oxide films as studied by x‐ray photoelectron spectroscopy and work‐function measurements. *J. Appl. Phys.* 73, 4344-4350 (1993).
9. G. P. Lopez, D. G. Castner, B. D. Ratner, Xps O 1s Binding-Energies for Polymers Containing Hydroxyl, Ether, Ketone and Ester Groups. *Surf. Interface Anal.* 17, 267-272 (1991).
10. H. G. Yang, S. B. Xu, L. Jiang, Y. Dan, Thermal Decomposition Behavior of Poly (Vinyl Alcohol) with Different Hydroxyl Content. *J. Macromol. Sci., Part B: Phys.* 51, 464-480 (2012).
11. W. L. Huang, M. H. Hsu, S. P. Chang, S. J. Chang, Y. Z. Chiou, Indium Gallium Oxide Thin Film Transistor for Two-Stage UV Sensor Application. *ECS J. Solid State Sci. Technol.* 8, Q3140-Q3143 (2019).
12. J. Sheng, E. J. Park, B. Shong, J. S. Park, Atomic Layer Deposition of an Indium Gallium Oxide Thin Film for Thin-Film Transistor Applications. *ACS Appl. Mater. Interfaces* 9, 23934-23940 (2017).
13. J. H. Park*, et al.*, Structural and Electrical Properties of Solution-Processed Gallium-Doped Indium Oxide Thin-Film Transistors. *Jpn. J. Appl. Phys.* 50, 080202 (2011).
14. C. H. Choi, Y. W. Su, L. Y. Lin, C. C. Cheng, C. H. Chang, The effects of gallium on solution-derived indium oxide-based thin film transistors manufactured on display glass. *Rsc Adv.* 5, 93779-93785 (2015).
15. J. H. Park*, et al.*, Enhanced performance of solution-processed amorphous gallium-doped indium oxide thin-film transistors after hydrogen peroxide vapor treatment. *Appl. Phys. Express* 7, 051101 (2014).
16. Y. H. Kang*, et al.*, Two-component solution processing of oxide semiconductors for thin-film transistors via self-combustion reaction. *J. Mater. Chem. C* 2, 4247-4256 (2014).
17. K. H. Lee*, et al.*, Modulation of aqueous precursor solution temperature for the fabrication of high-performance metal oxide thin-film transistors. *Appl. Phys. Express* 8, 081101 (2015).
18. M. T. Lusk, R. T. Collins, Z. Nourbakhsh, H. Akbarzadeh, Quantum confinement of nanocrystals within amorphous matrices. *Phys. Rev. B* 89, 075433 (2014).
19. J. E. Medvedeva, D. B. Buchholz, R. P. H. Chang, Recent Advances in Understanding the Structure and Properties of Amorphous Oxide Semiconductors. *Adv. Electron. Mater.* 3, 1700082 (2017).

20. T. Kamiya, H. Hosono, Roles of Hydrogen in Amorphous Oxide Semiconductor. *ECS Trans.* 54, 103-113 (2013).
21. T. Kamiya, K. Nomura, H. Hosono, Origins of High Mobility and Low Operation Voltage of Amorphous Oxide TFTs: Electronic Structure, Electron Transport, Defects and Doping. *J. Disp. Technol.* 5, 273-288 (2009).
22. H. J. Kim*, et al.*, The self-activated radical doping effects on the catalyzed surface of amorphous metal oxide films. *Sci. Rep.* 7, 12469 (2017).
23. J. Socratous*, et al.*, Electronic Structure of Low-Temperature Solution-Processed Amorphous Metal Oxide Semiconductors for Thin-Film Transistor Applications. *Adv. Funct. Mater.* 25, 1873-1885 (2015).
24. X. D. Li, S. Y. Chen, T. P. Chen, Y. Liu, Thickness Dependence of Optical Properties of Amorphous Indium Gallium Zinc Oxide Thin Films: Effects of Free-Electrons and Quantum Confinement. *Ecs Solid State Lett.* 4, P29-P32 (2015).
25. X. D. Li*, et al.*, A study on the evolution of dielectric function of ZnO thin films with decreasing film thickness. *J Appl. Phys.* 115, 103512 (2014).
26. E. S. M. Goh, T. P. Chen, C. Q. Sun, Y. C. Liu, Thickness effect on the band gap and optical properties of germanium thin films. *J. Appl. Phys.* 107, 024305 (2010).
27. W. Huang*, et al.*, Metal Composition and Polyethylenimine Doping Capacity Effects on Semiconducting Metal Oxide-Polymer Blend Charge Transport. *J Am. Chem. Soc.* 140, 5457-5473 (2018).
28. S. L. Moffitt*, et al.*, Probing the Unique Role of Gallium in Amorphous Oxide Semiconductors through Structure-Property Relationships. *Adv. Electron. Mater.* 3, 1700189 (2017).
29. X. Yu*, et al.*, Ultra-flexible, "invisible" thin-film transistors enabled by amorphous metal oxide/polymer channel layer blends. *Adv. Mater.* 27, 2390-2399 (2015).
30. W. Huang*, et al.*, Metal Oxide Transistors via Polyethylenimine Doping of the Channel Layer: Interplay of Doping, Microstructure, and Charge Transport. *Adv. Funct. Mater.* 26, 6179-6187 (2016).
31. D. B. Buchholz*, et al.*, The Structure and Properties of Amorphous Indium Oxide. *Chem. Mater.* 26, 5401-5411 (2014).
32. G. Kresse, J. Hafner, Ab initio molecular-dynamics simulation of the liquid-metal-amorphous-semiconductor transition in germanium. *Phys. Rev. B* 49, 14251-14269 (1994).
33. G. Kresse, J. Hafner, Ab initio molecular dynamics for liquid metals. *Phys. Rev. B* 47, 558-561 (1993).
34. G. Kresse, J. Furthmuller, Efficient iterative schemes for ab initio total-energy calculations using a plane-wave basis set. *Phys. Rev. B* 54, 11169-11186 (1996).
35. G. Kresse, J. Furthmuller, Efficiency of ab-initio total energy calculations for metals and semiconductors using a plane-wave basis set. *Comp Mater Sci* 6, 15-50 (1996).
36. P. Hohenberg, W. Kohn, Inhomogeneous Electron Gas. *Phys. Rev. B* 136, B864-+ (1964).
37. W. Kohn, L. J. Sham, Self-Consistent Equations Including Exchange and Correlation Effects. *Phys Rev* 140, 1133-& (1965).
38. J. P. Perdew, K. Burke, M. Ernzerhof, Generalized Gradient Approximation Made Simple. *Phys. Rev. Lett.* 77, 3865-3868 (1996).
39. J. P. Perdew, K. Burke, M. Ernzerhof, Generalized Gradient Approximation Made Simple [Phys. Rev. Lett. 77, 3865 (1996)]. *Phys. Rev. Lett.* 78, 1396-1396 (1997).
40. P. E. Blochl, Projector augmented-wave method. *Phys. Rev. B* 50, 17953-17979 (1994).
41. G. Kresse, D. Joubert, From ultrasoft pseudopotentials to the projector augmented-wave method. *Phys. Rev. B* 59, 1758-1775 (1999).

42. R. Hoppe, The Coordination Number– an“Inorganic Chameleon”. *Angew. Chem., Int. Ed. Engl.* 9, 25-34 (1970).
43. R. Hoppe*, et al.*, A New Route to Charge-Distributions in Ionic Solids. *J Less-Common Met* 156, 105-122 (1989).
44. R. Khanal, D. B. Buchholz, R. P. H. Chang, J. E. Medvedeva, Composition-dependent structural and transport properties of amorphous transparent conducting oxides. *Phys. Rev. B* 91, 205203 (2015).
45. K. Momma, F. Izumi, VESTA 3for three-dimensional visualization of crystal, volumetric and morphology data. *J. Appl. Crystallogr.* 44, 1272-1276 (2011).
46. J. Heyd, J. E. Peralta, G. E. Scuseria, R. L. Martin, Energy band gaps and lattice parameters evaluated with the Heyd-Scuseria-Ernzerhof screened hybrid functional. *J Chem. Phys.* 123, 174101 (2005).
47. J. Heyd, G. E. Scuseria, M. Ernzerhof, Hybrid functionals based on a screened Coulomb potential. *J. Chem. Phys.* 118, 8207-8215 (2003).
48. J. J. Meléndez, M. Wierzbowska, In2O3 Doped with Hydrogen: Electronic Structure and Optical Properties from the Pseudopotential Self-Interaction Corrected Density Functional Theory and the Random Phase Approximation. *J Phys. Chem. C* 120, 4007-4015 (2016).
49. S. Limpijumnong, P. Reunchan, A. Janotti, C. G. Van de Walle, Hydrogen doping in indium oxide: An ab initiostudy. *Phys. Rev. B* 80, 193202 (2009).
50. J. E. Medvedeva*, et al.*, Origin of high carrier concentration in amorphous wide-bandgap oxides: Role of disorder in defect formation and electron localization in In2O3−x. *J. Appl. Phys.* 127, 175701 (2020).
51. C. Jones, The stabilisation and reactivity of indium trihydride complexes. *Chem. Commun.*, 2293-2298 (2001).
52. J. W. Hennek*, et al.*, Oxygen "getter" effects on microstructure and carrier transport in low temperature combustion-processed a-InXZnO (X = Ga, Sc, Y, La) transistors. *J Am. Chem. Soc.* 135, 10729-10741 (2013).
53. B. H. Wang*, et al.*, Marked Cofuel Tuning of Combustion Synthesis Pathways for Metal Oxide Semiconductor Films. *Adv. Electron. Mater.* 5, 1900540 (2019).
54. B. Wang*, et al.*, Expeditious, scalable solution growth of metal oxide films by combustion blade coating for flexible electronics. *Proc. Natl. Acad. Sci. U. S. A.* 116, 9230-9238 (2019).